

## Article

# Chemically Modified TiO<sub>2</sub> Photocatalysts as an Alternative Disinfection Approach for Municipal Wastewater Treatment Plant Effluents

Dimitrios S. Tsoukleris <sup>1</sup>, Maria-Anna Gatou <sup>1,\*</sup>, Nefeli Lagopati <sup>1,2</sup>, Labrini Sygellou <sup>3</sup>,  
Dionysios C. Christodouleas <sup>4</sup>, Polycarpos Falaras <sup>5</sup> and Evangelia A. Pavlatou <sup>1,\*</sup>

<sup>1</sup> Laboratory of General Chemistry, School of Chemical Engineering, National Technical University of Athens, Zografos Campus, 15772 Athens, Greece; dtsoukleris@gmail.com (D.S.T.); nlagopati@med.uoa.gr (N.L.)

<sup>2</sup> Laboratory of Biology, Department of Basic Medical Sciences, Medical School, National and Kapodistrian University of Athens, 11527 Athens, Greece

<sup>3</sup> Foundation of Research and Technology Hellas, Institute of Chemical Engineering Sciences, Platani, 26504 Patras, Greece; sygellou@iceht.forth.gr

<sup>4</sup> Department of Chemistry, University of Massachusetts Lowell, Lowell, MA 01854, USA; dionysios\_christodouleas@uml.edu

<sup>5</sup> Institute of Nanoscience and Nanotechnology, National Center for Scientific Research "Demokritos", Agia Paraskevi, 15310 Athens, Greece; p.falaras@inn.demokritos.gr

\* Correspondence: mgatou2@mail.ntua.gr (M.-A.G.); pavlatou@chemeng.ntua.gr (E.A.P.)

**Citation:** Tsoukleris, D.S.; Gatou, M.-A.; Lagopati, N.; Sygellou, L.; Christodouleas, D.C.; Falaras, P.; Pavlatou, E.A. Chemically Modified TiO<sub>2</sub> Photocatalysts as an Alternative Disinfection Approach for Municipal Wastewater Treatment Plant Effluents. *Water* **2023**, *15*, 2052. <https://doi.org/10.3390/w15112052>

Academic Editors: Evangelos Karvelas, Ioannis Sarris and Theodoros Karakasidis

Received: 3 April 2023

Revised: 22 May 2023

Accepted: 26 May 2023

Published: 28 May 2023



**Copyright:** © 2023 by the authors. Licensee MDPI, Basel, Switzerland. This article is an open access article distributed under the terms and conditions of the Creative Commons Attribution (CC BY) license (<https://creativecommons.org/licenses/by/4.0/>).

**Abstract:** Among key issues in municipal wastewater treatment plants (MWTP) is the existence of pathogenic bacteria in the discarded effluents. Conventional disinfectants (ozone, UV irradiation, chlorine) have been insufficient in providing safe water due to the development of undesirable and noxious by-products. TiO<sub>2</sub> comprises an attractive alternative to conventional methods because of its versatility and recently explored biocidal efficiency. As a result, within the framework of this study, chemically modified, visible active nanocrystalline TiO<sub>2</sub> powders (N-TiO<sub>2</sub>, N,S-TiO<sub>2</sub>, and Ag@N-TiO<sub>2</sub>) were prepared via a low-cost, feasible sol-gel method for the treatment of real municipal wastewater effluents. Wastewater samples were acquired from the outlet of the treatment of Antiparos (Cyclades, Greece) MWTP during the summer period in which a great number of seasonal habitants and tourists usually visit the island, resulting in at least a doubling of the population. All synthesized powders were thoroughly characterized using various morphological and spectroscopic techniques, such as FE-SEM, XRD, micro-Raman, FTIR, DLS, UV-DRS, and XPS. Photocatalytic evaluation experiments were initially conducted towards Rhodamine B degradation under visible light irradiation. Among all studied powders, Ag@N-TiO<sub>2</sub> indicated the highest efficiency, reaching total degradation (100%) of RhB within 240 min due to its smaller crystallite size (1.80 nm), enhanced surface area (81 m<sup>2</sup>g<sup>-1</sup>), and reduced energy band gap (E<sub>g</sub> = 2.79 eV). The effect of the produced powders on the disinfection as assessed in terms of fecal indicator microorganisms (*E. coli* and total coliforms) inactivation was also examined in a semi-pilot scale-up photocatalytic reactor. Ag@N-TiO<sub>2</sub> nanopowder was also found substantially more active for both groups of bacteria, leading to complete inactivation in less than 35 min, probably due to the higher production of H<sub>2</sub>O<sub>2</sub>/•OH, as emerged from the photocatalytic mechanism study. In addition, Ag@N-TiO<sub>2</sub> nanoparticles demonstrated excellent photocatalytic and disinfection stability even after five subsequent recycling trials (8.34% activity loss and complete inactivation, respectively). The results of the present study demonstrate the feasibility for Ag@N-TiO<sub>2</sub> to be utilized as a viable, eco-friendly approach for the photocatalytic pathogenic bacteria inactivation as an alternative disinfection approach for municipal wastewater treatment plant effluents with intense seasonal fluctuations in volume.

**Keywords:** Ag@N-doped TiO<sub>2</sub>; bacterial disinfection; chemically modified TiO<sub>2</sub>; effluents; N-doped TiO<sub>2</sub>; N,S-codoped TiO<sub>2</sub>; titanium dioxide; visible light irradiation; WWTP

## 1. Introduction

Municipal wastewater treatment plants (MWTP) are key facilities in cities around the world where about 350 billion m<sup>3</sup> of wastewater is globally treated every year [1]. Besides mitigating environmental pollution, wastewater treatment plants can produce water for use in agricultural irrigation [2–4]. The produced water should, however, be free of (a) waterborne pathogens (i.e., helminths, protozoa, fungi, bacteria, and viruses), which are typically present in untreated wastewaters and should be eliminated during the treatment process, and (b) toxic byproducts that might be produced during the wastewaters' treatment itself. For more than two decades, photocatalysis has been identified as an advanced oxidation process/technology (AOP/AOT) that can be used for wastewater treatment, and hundreds of research studies have described new photocatalysts [5–7], but, in practice, the photocatalytic systems have only found very limited practical applications [8], due to the necessity for treatment of heavily polluted water effluents (without being treated with any method), the limited testing of photocatalytic systems in realistic conditions (e.g., real effluents of MWTP), and the absence of carefully designed reactors that can facilitate inline, continuous treatment of large volumes of effluents of MWTPs. Previous research studies, for example, have tested the performance of various photocatalysts for bacterial inactivation in small standard solutions [7], rather than large volumes of effluents from a MWTP that could provide more meaningful conclusions. In fact, useful conclusions for the practical applications of photocatalysis could be extracted only when real effluents of a MWTP are treated in large tanks using a continuous process because in real settings (a) the composition of wastewaters is significantly more complex than standard bacterial solutions (typically prepared in buffer) and may contain scavengers that can inactivate the radicals produced during the photocatalytic process [8]; (b) large volumes of wastewaters must be disinfected inside a robust reactor (made of concrete, metal, etc.), where irradiation and aeration of the whole body could be challenging; (c) the disinfection process should be as short as possible, continuous, efficient and compatible with the other steps of the wastewater pretreatment. In this framework, the performance evaluation of the photocatalysts for bacteria inactivation of real wastewater effluents of a municipality treatment plan is of high priority. In addition, it is necessary to determine the efficiency of the treatment process in realistic conditions by performing the investigation in a carefully designed photocatalytic tank, which is a scale model of a larger system that could be connected in line to a MWTP.

Municipal wastewater treatment plants are designed to serve a more or less stable population and large fluctuations in the volume of wastewater may cause problems in the performance of wastewater treatment plants. Islands that attract vacationers host a large influx of tourists during specific periods of the year so the increase of their population during specific periods stresses the wastewater treatment plants that typically work above their capacity.

The operative process in a typical municipal WWTP incorporates three basic stages: (a) a primary treatment where physical processes are utilized; solids, oils, fats, and organic matter are eliminated and wastewater is assembled for the next stage. Then, follows the next stage, that of (b) secondary treatment. Biological, as well as chemical, processes are integrated, leading to the further elimination of organic matter and suspended solids. During this stage, the majority of pollutants is removed. Various mechanisms, such as biological decomposition, sorption to suspended solids or incorporation into microbial communities, have been suggested for this stage. One of the most prevalent systems employed as secondary treatment is activated sludge, relying on the microbial oxidation of

organic compounds. Further treatments can be alternatively conducted, (c) tertiary or advanced processes. These commonly constitute a combination of processes provoking the removal of suspended residual solids through filtration with sand, gravel, or anthracite coal, as well as the disinfection of the wastewater effluents via chlorination, ozonation, UV-radiation, etc. prior to discharge [9]. Figure S1 outlines the usual treatment process applied in a typical WWTP.

Chlorination, ultraviolet (UV) irradiation, and ozonation are the most commonly employed conventional techniques during the disinfection phase due to their extent of use, relative efficiency, and popularity [10–12]. On the whole, these three methods possess the adequacy to inactivate an extensive range of pathogenic microorganisms to a sufficient rate [13], whilst this is not the only factor that should be assessed. Until today, researchers [14] have already ascertained a series of attributes that an optimal disinfectant should retain, involving toxicity to organisms, solubility, stability, consistency, interaction with various substances, corrosion, deodorizing ability, wide availability, and cost. Thus far, none of the disinfection agents or techniques for the aforementioned objectives has thoroughly fulfilled these parameters, rendering it obligatory to delve into other materials and methods.

Chlorination is by far the most popular technique [15], as it comprises an eminent technology. The major reasons are low cost (in comparison to others), proven effectiveness, and application with no distinguished equipment needed [16]. Furthermore, this method is characterized by a vast utility for being used to domestic, as well as industrial, applications. On the other hand, utilization of UV irradiation has been confined due to increased operating costs and the requirement of specialized infrastructure [17]. As for ozonation [11,18,19], existing studies [20] declare that ozone possesses enhanced efficiency, proportionated to the other disinfection methods, in the matter of disinfection towards viruses, bacteria and protozoa, with distinctly high efficacy [21]. Nevertheless, prime investment requirements, the usage intricacy, infrastructure requirements, as well as operating costs, compose significant limitations for the utilization of ozone disinfection as an endorsed technology [13].

A consequential drawback frequently ascribed to these conventional methods is the formation of byproducts throughout their application, consisting of acetonitriles, bromohydrines, chlorophenols, haloacetic acids, halurofuranones, and n-chloramines, that are considered as potential human carcinogens, given their high reactivity [13,21]. Even though there is no indisputable evidence on the association between the exposure to these compounds and the mutagenic effects on humans, a great number of trials in animals have been conducted, intimating the adequate evidence of carcinogenic and/or teratogenic effect on both germinal and neurological cells [22–25]. Hence, the provocation to be faced is the inspection of alternative methods to fulfil the characteristics of an ideal disinfectant.

Advanced oxidation processes (AOPs) have been identified as a technology that could be used in the disinfection phase of wastewater treatment plants [3,26–28]. Several materials have been explored as photocatalysts for such applications, like hexaferrites and MOFs, presenting highly satisfactory results [29–31]. However, TiO<sub>2</sub> has received great attention in recent years [3,32–34], as it is well established that when photons from a light source interact with the surface of a TiO<sub>2</sub> particle, electrons can be excited from the valance to conduction band, leaving behind positively charged holes. The electrons react with molecular oxygen and the positive holes with water molecules so various types of reactive oxygen species (ROS) are formed and kill bacteria [35,36]. Some previous research efforts have evaluated the photocatalytic performance of TiO<sub>2</sub> photocatalysts (pure or chemically doped) by testing the bacteria disinfection rates when a photocatalyst reacts with standard solutions of bacteria contained in small containers (e.g., tubes, vials) under visible light irradiation [37,38].

To address the above issues, in this study, we evaluated the performance of several photocatalysts for the decontamination of real wastewater effluents in the municipality treatment plant of Antiparos, Greece. In addition, we have designed and fabricated a

semi-pilot scale-up photocatalytic reactor (volume capacity = 5 L), which could be an in-scale model of a larger reactor, and synthesized three different TiO<sub>2</sub>-based photocatalytic materials (i.e., TiO<sub>2</sub> doped with nitrogen (N-doped TiO<sub>2</sub>), TiO<sub>2</sub> co-doped with nitrogen and sulfur (N,S doped-TiO<sub>2</sub>), and silver modified TiO<sub>2</sub> doped with nitrogen (Ag@N-doped TiO<sub>2</sub>)) and tested the performance of the materials for the disinfection of fecal coliforms bacteria present in effluents after the stabilization pond of the municipality wastewater treatment plant of Antiparos, Greece.

The novelty of this study hence lies in the evaluation of the aforementioned powders regarding their photocatalytic disinfection efficiency towards pathogenic bacteria (*E. coli* and total coliforms) present in real wastewater effluents originating from Antiparos MWTP (Cyclades, Greece), utilizing a semi-pilot scale-up photocatalytic reactor.

## 2. Materials and Methods

### 2.1. Preparation of the Chemically Modified TiO<sub>2</sub> Powders

*Synthesis of N-doped TiO<sub>2</sub>*: An amount of 20 mL of titanium (IV) butoxide (C<sub>16</sub>H<sub>36</sub>O<sub>4</sub>Ti, 97%, Sigma-Aldrich, Darmstadt, Germany) was poured in 100 mL aqueous solution acidified with nitric acid (HNO<sub>3</sub>, 65%, Penta, Prague, Czech Republic) (pH < 2) under vigorous stirring and then 30 mL of 1-butanol (CH<sub>3</sub>(CH<sub>2</sub>)<sub>3</sub>OH, 99.8%, Sigma-Aldrich, Darmstadt, Germany) was added to produce a translucent TiO<sub>2</sub> colloidal solution. An addition of 25 g of urea (CH<sub>4</sub>N<sub>2</sub>O, 99%, Sigma-Aldrich, Darmstadt, Germany) was made under vigorous stirring that lasted until the complete evaporation of the solvent and the final production of a gel. The gel was thermally treated at 450°C for 4 h, triturated and purified through rinsing and centrifugation for removing impurities, and then a yellowish powder was acquired (Figure 1a).

*Synthesis of N,S-doped TiO<sub>2</sub>*: An amount of 20 mL of titanium (IV) butoxide (C<sub>16</sub>H<sub>36</sub>O<sub>4</sub>Ti, 97%, Sigma-Aldrich, Darmstadt, Germany) was added in 100 mL aqueous solution acidified with nitric acid (HNO<sub>3</sub>, 65%, Penta, Prague, Czech Republic) (pH < 2) under vigorous stirring and then 30 mL of 1-butanol (CH<sub>3</sub>(CH<sub>2</sub>)<sub>3</sub>OH, 99.8%, Sigma-Aldrich, Darmstadt, Germany) was added to produce a translucent TiO<sub>2</sub> colloidal solution. An amount of 15 g of thiourea (CH<sub>4</sub>N<sub>2</sub>S, 99%, Sigma-Aldrich, Darmstadt, Germany) was then added under vigorous stirring until the solvent was completely evaporated, leading to the production of a gel. The gel was heated at 450°C for 4 h, triturated, and through rinsing and centrifugation for removing impurities, a yellow-colored powder was finally retrieved (Figure 1b).

*Synthesis of Ag@N-doped TiO<sub>2</sub>*: The particles of N-doped TiO<sub>2</sub>, that were produced following the aforementioned protocol were then mixed with 50 mL 0.75% *w/v* silver nitrate solution (AgNO<sub>3</sub>, 99.5%, Sigma-Aldrich, Darmstadt, Germany). After stirring at ambient temperature for 30 min, the suspension was conveyed into a Teflon-lined stainless-steel autoclave and was hydrothermally processed at 130°C for 3 h. Afterwards, the precipitate was dried at 120°C, rinsed with distilled water, and then heated at 70°C overnight. The silver-loaded nitrogen-doped TiO<sub>2</sub> powder had a greyish color (Figure 1c).

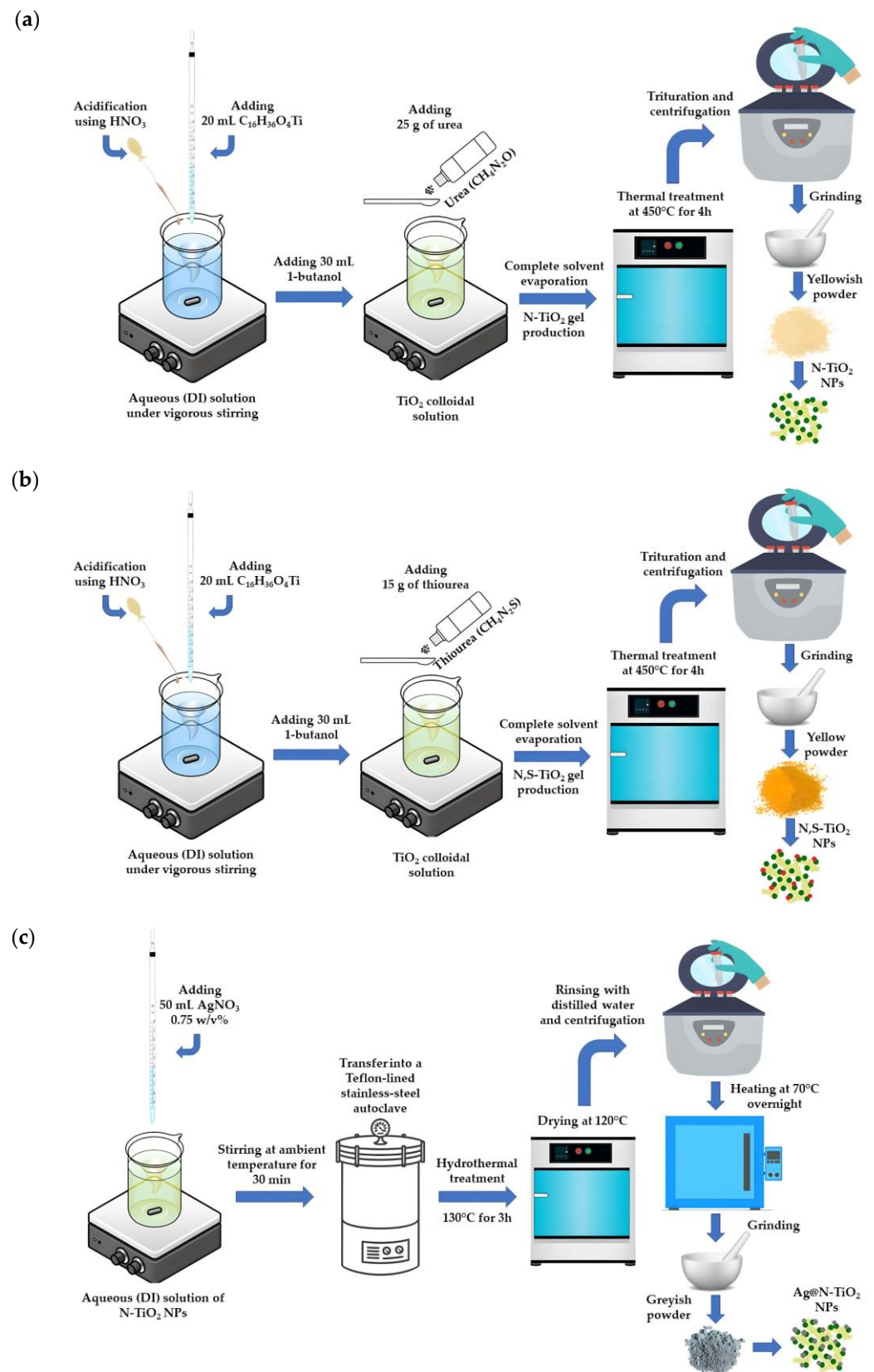


**Figure 1.** Schematic representation for the synthesis of (a) N-doped  $\text{TiO}_2$ , (b) N,S-codoped  $\text{TiO}_2$ , and (c) Ag-loaded N-doped  $\text{TiO}_2$  powder, respectively.

## 2.2. Case Study

A representative example of an island that faces an influx of tourists during summer months is Antiparos Island in Greece. The MWTP of Antiparos Island is located at Sifneikos Gyalos (500 m from the Antiparos settlement) and occupies an area of 28,400 m<sup>2</sup>. The mean daily design capacity of the WWTP is 240 m<sup>3</sup>/d during winter (1500 p.e.) and 480 m<sup>3</sup>/d during summer (3000 p.e.). The MWTP involves five stages, Steps A–E, performed in line (Figure 2). Step A (preliminary treatment) removes coarse solids and other large materials by grits and coarse. Step B (primary treatment) removes organic as well as inorganic solids by sedimentation, in addition to removing floating materials by skimming [39]. Step C (secondary treatment) uses aerobic microorganisms to further treat an effluent to remove the residual organics and the remaining suspended solids. Step D (tertiary treatment) removes specific wastewater constituents, such as nitrogen, phosphorus, additional suspended solids, refractory organics, heavy metals, and dissolved solids, that could not be removed by secondary treatment [40]. Step E (disinfection phase) inactivates waterborne pathogens in treated wastewater that last ~40 min.

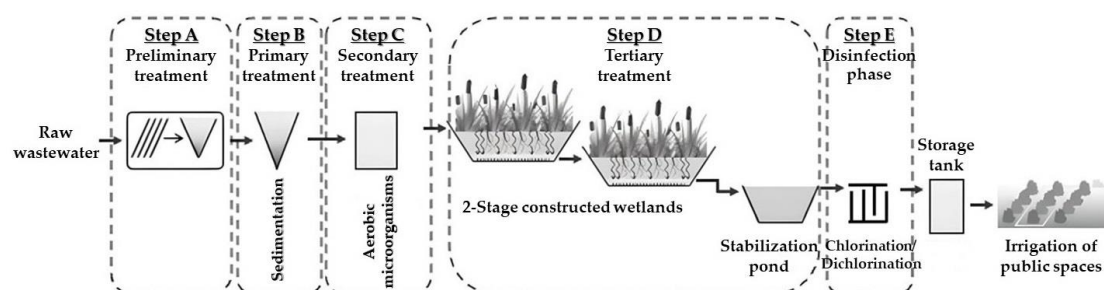


**Figure 2.** Schematic representation of the five-step treatment process followed in the municipal wastewater treatment plant of Antiparos, Greece.

During the summer, the MWTP works over capacity and the complete disinfection of effluents is challenging. For instance, during October–March, the real capacity is 70–100 m<sup>3</sup>/day (400–600 habitants), while in the peak holiday season (July–August), it rises to ~250–450 m<sup>3</sup>/day (2500–5500 habitants and visitors). This means that the biological treatment plant is not able to overcome this intense fluctuation in population given that, due to a large flow of sewage, the contact time of the chlorine with the sewage is dramatically limited, resulting in ineffective disinfection.

## 2.3. Municipal Wastewater Treatment Plant (MWTP) Samples

Real samples were gathered from the municipal wastewater treatment plant of Antiparos Municipality (Greece). The facility treats the wastewater from a population of 1211 residents and generates 131.400 m<sup>3</sup> of secondary effluents on average per year. Table 1 includes information regarding the chemical composition and bacterial load of the secondary effluents of this wastewater treatment plant after tertiary treatment (STEP D).

**Table 1.** Chemical parameters and bacterial load of tertiary effluents originating from Antiparos MWTP, collected during the summer period.

Parameter	Average Value *
Chemical Oxygen Demand (COD)	34 ± 3 mg/L
Biochemical Oxygen Demand (BOD)	14 ± 2 mg/L
Total Suspended Solids (TSS)	11.0 ± 0.6 mg/L
Nitrate (NO <sub>3</sub> <sup>-</sup> )	1.5 ± 0.2 mg/L
Nitrite (NO <sub>2</sub> <sup>-</sup> )	1.100 ± 0.003 mg/L
Phosphate (PO <sub>4</sub> <sup>3-</sup> )	2.100 ± 0.005 mg/L
<i>E. coli</i>	1400 CFU/mL

Note: \* All experiments for the calculation of each studied parameter have been conducted thrice.

#### 2.4. Characterization of the Chemically Modified TiO<sub>2</sub> Powders

The morphology of the TiO<sub>2</sub>-based powders was analyzed using field emission SEM (FESEM, JSM-7401F, JEOL, Tokyo, Japan).

The X-ray diffractometer that was utilized to study the crystallinity of the prepared chemically modified powders was a Bruker D8 Advance (Bruker, Germany) with a CuK $\alpha$  radiation ( $\lambda = 1.5406 \text{ \AA}$ ) at a voltage of 40 kV and a current of 40 mA. The measurement was conducted at a 2 theta ( $2\theta$ ) angle ranging between 20 and 90° with a counting diffraction intensity step 0.01° per 1.0 s.

The FTIR spectra were collected in the 400–4000 cm<sup>-1</sup> range, with a resolution equal to 4 cm<sup>-1</sup> at room temperature by utilizing a FTIR JASCO4200 (Oklahoma City, Oklahoma, United States) instrument equipped by a Ge crystal.

In order to complement the FTIR data, Raman spectroscopy was conducted in the present study using a micro-Raman apparatus (inVia, Renishaw, Wotton-under-Edge, Gloucester, UK) provided with a green laser line ( $\lambda = 532 \text{ nm}$ ) as the excitation source with an average output power of 50 mW, approximately. Raman spectra were collected at room temperature, while an internal Si reference was used as the calibration of frequency shift value. A number of 3 to 10 spots were acquired for each measured powder. For recording Raman spectra, the following conditions were set for each sample: exposure time 30 s, accumulations equal to 3, power 1%, spectral range 100–1000 cm<sup>-1</sup>, and the spectral resolution for all measurements was 2 cm<sup>-1</sup>.

N<sub>2</sub> adsorption of synthesized powders was conducted in a ChemBET 3000 Instrument (Yumpu, Diepoldsau, Switzerland) to determine the specific surface area BET. Initially, each sample endured a degassing procedure at 80°C for 24 h.

X-ray photoelectron spectroscopy (XPS) (Leybold SPECS LHS/EA10, Leybold GmbH, Cologne, Germany) was applied to estimate the surface chemical states of the samples. An ultra-high vacuum system (UHV) equipped with an X-ray gun was used for XPS measurements. An unmonochromatized MgK $\alpha$  line at 1253.6 eV and two analyzer pass energies of 15 eV (giving a full width at half maximum (FWHM) of 0.85 eV for the Ag 3d5/2 peak) and 40 eV were used. A fitting routine was used for analyzing the XPS core level spectra, resulting in the decomposition of each spectrum into individual mixed Gaussian–Lorentzian peaks after a Shirley background subtraction. Errors concerning peak areas are found in the range of  $\approx 10\%$ , while the accuracy for binding energies' (BEs) assignments is  $\approx 0.1 \text{ eV}$ . The measured samples were initially in powder form and pressed into a pellet and the analyzed area was a 7.0 mm diameter spot. In total, XPS spectra were recorded at 25°C.

Dynamic light scattering (DLS) was conducted to measure the hydrodynamic diameter and its distribution for all powders' particles that were immersed in distilled water solutions. The incident light was a 633 nm laser and the scattering angle of 173° was set for recording scattering intensity (Malvern Zetasizer Nano ZS, Malvern Panalytical Ltd., Malvern, UK). Energy band gap ( $E_g$ ) values were estimated by using an ultraviolet-visible (UV-Vis) spectrometer (Jasco UV/Vis/NIR Model name V-770, Interlab, Athens, Greece) equipped with an integrating sphere, permitting the recording of diffuse reflectance measurements.

The determination of silver ions' concentration during the silver leaching experiments was conducted using ICP-MS technique (7700, Perkin Elmer, Waltham, MA, USA).

The mineralization of RhB was ascertained through total organic carbon (TOC) analysis (TOC-LCSH/CSN, Shimadzu Scientific Instruments, Columbia, MD, United States) for the same time points as selected for the photocatalytic study experiments.



### 2.5. Photocatalytic Activity of the Chemically Modified TiO<sub>2</sub> Powders

The efficiency of the photocatalytic activity of the synthesized chemically modified TiO<sub>2</sub> powders under visible light irradiation was evaluated using 0.005 g of each powder (N-doped TiO<sub>2</sub>, N,S-codoped TiO<sub>2</sub>, and Ag-loaded N-doped TiO<sub>2</sub>) in 10 mg/L Rhodamine B (RhB) aqueous solution (250 mL) at 25°C and pH = 6.65 ± 0.01. Prior to each photocatalytic experiment (cycle), extra pure O<sub>2</sub> (99.999%) was vented through the RhB solution for 1h, in order to saturate it.

The utilized photoreactor was equipped with four parallel lamps at 10 cm distance over the powders' surface [41]. The lamps employed during the experimental procedure were 15 W visible lamps of 900 lumens (OSRAM GmbH, Munich, Germany). The resulting absorbance of the produced TiO<sub>2</sub> powders was measured using a Thermo Fisher Scientific Evolution 200 Spectrometer (Thermo Fisher Scientific, Waltham, MA, USA). The evaluation of the ratio of the measured A (absorption at each time) to the initial ( $A_{\text{initial}}$ ) facilitated the determination of the ratio  $C/C_0$ , where C is the concentration of RhB after a certain time of photocatalysis and  $C_0$  is the initial concentration of RhB determined at a wavelength equal to 554 nm [41].

### 2.6. Photocatalytic Reactor System

A custom-designed photocatalytic reactor system (Figure 3), which consisted of a properly designed rectangular concrete photocatalysis tank (100 × 50 × 10 cm) and a cylindrical concrete precipitation tank (d = 25 cm) with a conical bottom for optimal catalyst collection, were constructed, waterproofed, and used as a semi-pilot scale-up photocatalytic disinfection process of wastewater effluents. The photocatalytic tank had a volume capacity equal to 5 L. It was equipped with four air blowers to provide continuous aeration of the wastewater body (Figure 3A). Nine high-power Luxeon light-emitting diodes (LEDs) that emit light in the region of 440–460 nm ( $P = 4.5 \text{ mW cm}^{-2}$ ) were placed 20 cm over the tank to irradiate the wastewater samples.

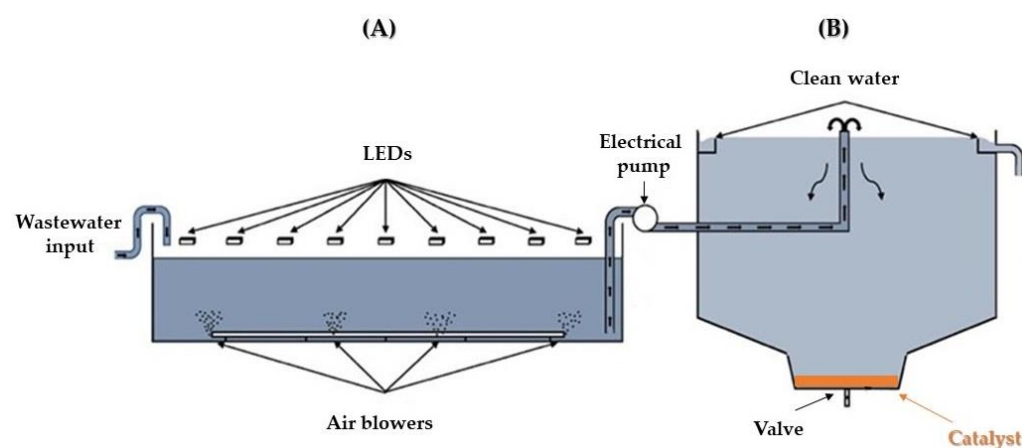


**Figure 3.** Schematic representation of the photocatalytic reactor consisted of (A) photocatalytic tank and (B) precipitation tank.

The precipitation tank (Figure 3B) was designed to collect the photocatalyst after the disinfection step. It had a capacity of 5 L. An opening at the side of the tank allowed the insertion of a tube to transfer the wastewater effluents from the photocatalysis tank to the precipitation tank. Openings close to the top of the tank allowed the collection of clean water. A suitably shaped valve was placed at the bottom of the cone of the tank to allow the collection of the photocatalyst (Figure 3B).



### 2.7. Photocatalytic Disinfection Experiments

Real samples were collected from the MWTP of Antiparos and more specifically, after performing the tertiary treatment step (Step D) (see Figure 2). A sufficient amount of wastewater was collected during the summer period (June), in order for all recorded experiments to be conducted thrice. An amount of 5 L of wastewater were added in the photocatalytic tank together with 5 g of the chemically modified TiO<sub>2</sub> powders and the photocatalytic disinfection of bacteria (*E. coli* and fecal coliforms were studied within the framework of this study) was performed [42]. After the end of the photocatalytic disinfection process, which lasted 40 min, the treated wastewater (that contained the suspended photocatalyst) was pumped to the precipitation tank, where it was allowed to rest for 60 min.

The photocatalysts were collected through the tank's bottom valve, so it could be reused without any further treatment for at least five times. The cleaned water was collected through a tube connected close to the top of the precipitation tank (Figure 2b).

### 2.8. Determination of the Concentration of Bacteria in Wastewaters

A Compact Dry™ EC (Nissui Pharma Solutions, Paris, France) coliform bacteria test kit (*EC test*) and a Compact Dry™ (Nissui Pharma Solutions, Paris, France) coliform bacteria test kit (*CF test*) were used to determine the concentration of bacteria (*E. coli* or fecal coliforms) present in samples collected from the top of the precipitation tank after their photocatalytic disinfection. The test kits contained test dishes prefilled with culture medium and other reagents. An amount of 1 mL of the tested sample was placed onto the center of the test dish and was incubated at 35 °C for 24 h to allow the formation of bacteria colonies. The bacteria colonies were counted manually, and the bacteria concentration was calculated in colony forming units (CFU) per 1 mL of each examined sample.

## 3. Results

### 3.1. Characterization of the Chemically Modified TiO<sub>2</sub> Powders

#### 3.1.1. XRD Analysis

XRD was utilized for studying the crystallinity of the developed chemically modified TiO<sub>2</sub> powders. Figure 4 presents the diffraction diagrams that emerged for the produced powders along with that of commercial TiO<sub>2</sub> (P25) acting as a reference sample. The salient TiO<sub>2</sub> crystal phase was anatase in all studied powder samples. The highest intensity diffraction peak of anatase (I<sub>A</sub>) in all samples was located at 2θ = 25.26°, acquiescing to (101) crystal plain, while the rest of anatase TiO<sub>2</sub> peaks detected accorded with the PDF No 03-065-5714 [43]. In the case of the N-doped TiO<sub>2</sub> sample, rutile (I<sub>R</sub>) was observed at 2θ = 27.36°, correlated with (110) crystal plain (PDF No 03-065-5714) [44]. The percentage of the rutile phase for the commercially available TiO<sub>2</sub> (P25) and N-doped TiO<sub>2</sub> is presented in Table 2 and was calculated according to Equation (1) [45]:

$$\%Rutile = \left( \frac{1}{1 + 0.884 \frac{I_{A(101)}}{I_{R(110)}}} \right) \times 100 \quad (1)$$

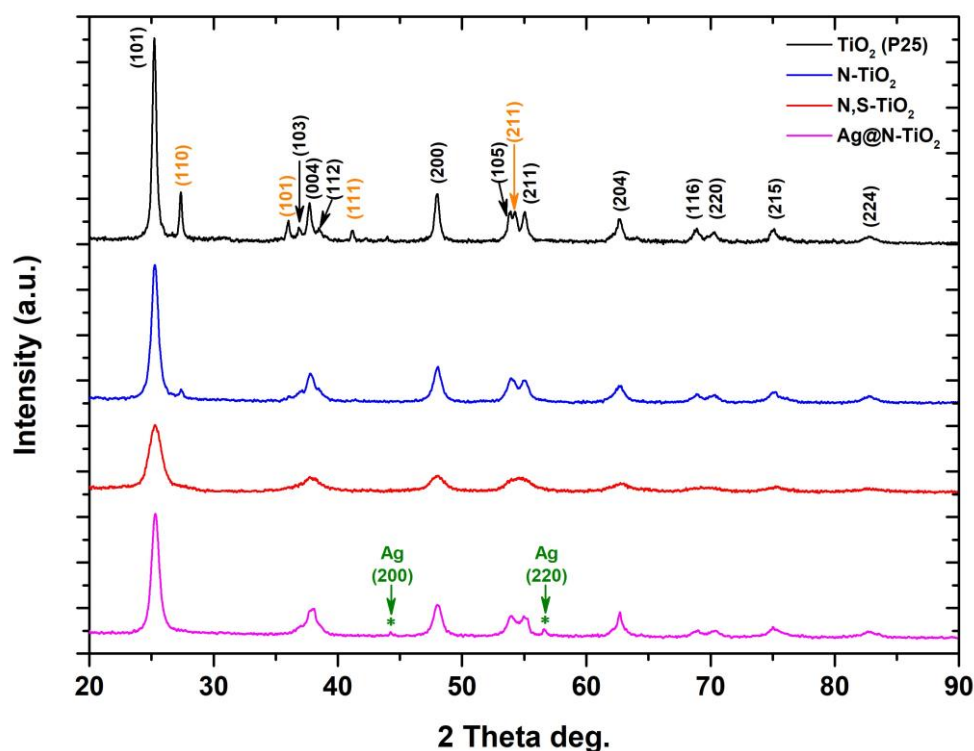


**Figure 4.** XRD pattern for the prepared chemically modified TiO<sub>2</sub> powders. The crystal planes presented in black correspond to the TiO<sub>2</sub> anatase phase, while the crystal planes presented in orange correspond to the TiO<sub>2</sub> rutile phase. An asterisk is used to indicate the presence of Ag in the case of the Ag@N-TiO<sub>2</sub> powder sample. The XRD pattern of commercial TiO<sub>2</sub> (P25) is presented as a reference.

**Table 2.** Crystallographic properties of the as-synthesized TiO<sub>2</sub> powders, as well as for commercial TiO<sub>2</sub> (P25) powder.

Sample	Crystalline Phase	Phases Percentage
TiO <sub>2</sub> (P25)	Tetragonal (anatase)	74.16%
	Tetragonal (rutile)	25.84%
N-doped TiO <sub>2</sub>	Tetragonal (anatase)	81.52%
	Tetragonal (rutile)	18.48%
N,S-doped TiO <sub>2</sub>	Tetragonal (anatase)	100%
Ag@N-doped TiO <sub>2</sub>	Tetragonal (anatase)	100%

As for N,S-codoped TiO<sub>2</sub> powder, only the crystalline structure of anatase TiO<sub>2</sub> phase was observed. More specifically, the (101), (004), (200), (105), (204), (116), (215), and (224) planes were verified [46]. In terms of Ag@N-doped TiO<sub>2</sub> powder, the peaks being present at 2 $\theta$  values of 44.22° and 56.56°, are indexed to (200) and (220) planes of Ag [47]. In addition, the crystal lattice indices, the crystallinity, and the average crystallite of the synthesized powders were calculated as demonstrated in Table 3. Moreover, the interplanar d-spacing calculations for commercial, N-doped, N,S-codoped, and Ag@N-doped TiO<sub>2</sub> powder are presented in detail in Tables S1, S2, S3, and S4, respectively.

**Table 3.** Crystal lattice indices, average crystallite size, FWHM, and crystallinity of the synthesized chemically modified TiO<sub>2</sub> powders.

Sample	Crystal Lattice Index			Average Crystallite Size (nm)	FWHM	Crystallinity (%)
	(a = b $\neq$ c)					
	a	b	c			

TiO <sub>2</sub> (P25)	3.7892	3.7892	9.5244	3.24	0.4238	68.19
N-TiO <sub>2</sub>	3.7825	3.7825	9.5147	2.13	0.6467	68.56
N,S-TiO <sub>2</sub>	3.7855	3.7855	9.5342	2.01	0.6846	70.03
Ag@N-TiO <sub>2</sub>	3.7833	3.7833	9.5050	1.80	0.7649	70.69

The mean crystallite size of the as-developed chemically modified TiO<sub>2</sub> powders was determined using the Debye–Scherrer equation (Equation (2)):

$$D = \frac{0.89\lambda}{\beta \cos \theta} \quad (2)$$

where  $\lambda$  = X-ray wavelength ( $\lambda = 1.5406 \text{ \AA}$ ), 0.89 accounts for Scherrer's constant,  $\beta$  stands for full width at half maximum (FWHM) of the anatase (101) plane's peak, and  $\theta$  represents Bragg's angle [48].

Additionally, interplanar d-spacing was predicted via Bragg's Law Equation (Equation (3)):

$$2d \sin \theta = n\lambda, n = 1 \quad (3)$$

Crystallinity index (CI%) was determined as indicated by Equation (4):

$$CI\% = \frac{\text{Area of all the crystalline peaks}}{\text{Area of all the crystalline and amorphous peaks}} \quad (4)$$

Crystal lattice index was verified through Equation (5) [49]:

$$\frac{1}{d_{hkl}^2} = \frac{h^2}{a^2} + \frac{k^2}{b^2} + \frac{l^2}{c^2} \quad (5)$$

No denoting alterations in the peak positions are spotted, as is evident from the corresponding XRD diffractograms. Nevertheless, variety among the intensity of the different samples can be detected, which affects the FWHM, leading to a crystallite size fluctuation. According to the aforementioned results, among the prepared samples, Ag@N-doped TiO<sub>2</sub> possesses the smallest mean crystallite size (~1.80 nm) (see Table 3). The crystallinity of the produced powders ranged between 68–71%.

### 3.1.2. FTIR Analysis

FTIR analysis of the chemically modified TiO<sub>2</sub> samples indicates the characteristics of the formation of relatively high purity TiO<sub>2</sub>. According to the FTIR spectra, several peaks at  $\approx 490$ , 1390, 1623, 1710, 2852, 2919, and 3410 cm<sup>-1</sup> are depicted (Figure 5).

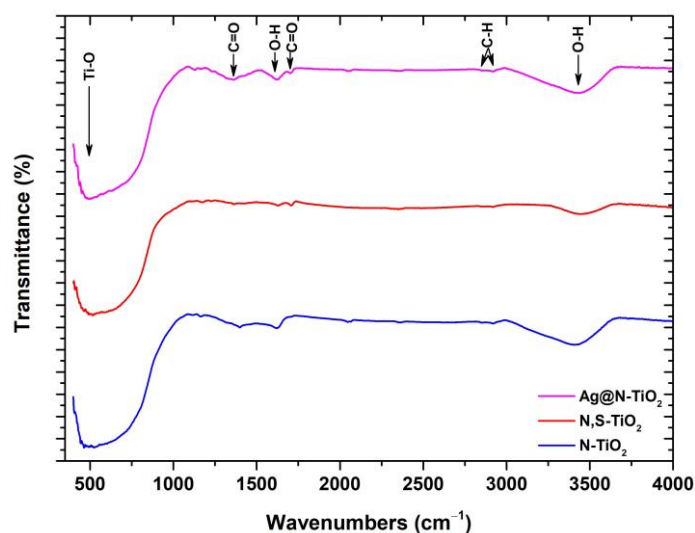


Figure 5. FTIR spectra of the chemically modified TiO<sub>2</sub> powders (at 25 °C).

The broad absorption band observed in the 400–1000  $\text{cm}^{-1}$  region is imputed to the Ti-O stretching of the oxygen bonds with two titanium atoms in nano-TiO<sub>2</sub> [50]. The peaks at  $\approx 1390$  and  $1710 \text{ cm}^{-1}$ , in the case of N,S-codoped TiO<sub>2</sub> and Ag@N-doped TiO<sub>2</sub> powder samples, can be assigned to the asymmetric stretching mode of titanium carboxylate [51]. Moreover, in all examined TiO<sub>2</sub> samples, the peak at  $1623 \text{ cm}^{-1}$ , along with the wide band between  $3200$  and  $3600 \text{ cm}^{-1}$ , indicate the bending of oxygen-hydrogen bonds and stretching modes of hydroxyl groups, respectively, confirming the existence of moisture in the examined samples [52].

The two frail bands located at  $2852$  and  $2919 \text{ cm}^{-1}$  are related to the characteristic frequencies of residual organic species, derived from the precursors used during the synthetic process, that were incompletely removed after washing the as-synthesized TiO<sub>2</sub> powders with distilled water. As a result, these bands can be imputed to C-H stretching vibrations of alkane groups [51].

### 3.1.3. Micro-Raman Analysis

The Raman spectra acquired from the chemically modified TiO<sub>2</sub> powders are presented in Figure 6.

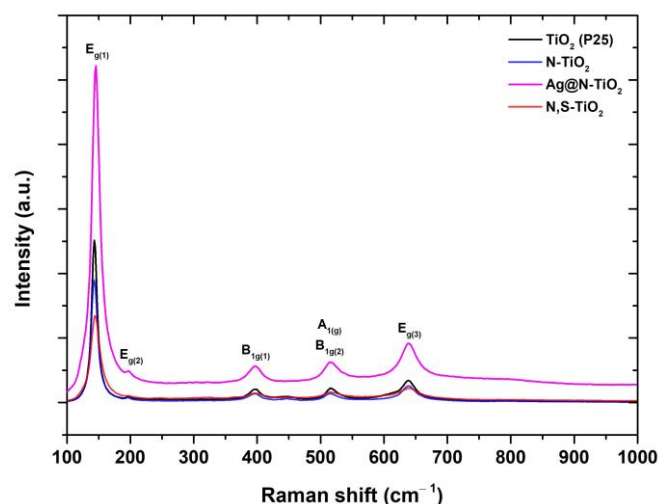


**Figure 6.** Raman spectra of chemically modified TiO<sub>2</sub> powders. The Raman spectra of commercial TiO<sub>2</sub> (P25) are used as a reference.

In the spectra of all the studied TiO<sub>2</sub> powders, the prevalent Raman active modes can be attributed to anatase TiO<sub>2</sub> phase. In particular, a peak characterized by strong intensity is spotted at approximately  $145 \text{ cm}^{-1}$  ( $E_{g(1)}$ ), followed by peaks of lower intensity at  $196 \text{ cm}^{-1}$  ( $E_{g(2)}$ ),  $398 \text{ cm}^{-1}$  ( $B_{1g(1)}$ ),  $515 \text{ cm}^{-1}$  (coupling of  $A_{1g}$  and  $B_{1g(2)}$  that overlap at room temperature), and  $639 \text{ cm}^{-1}$  ( $E_{g(3)}$ ) (see Figure 6). The position of  $E_{g(1)}$  Raman mode for the three studied chemically modified TiO<sub>2</sub> powders varies from  $143$  to  $146 \text{ cm}^{-1}$ , as seen in Figure 5. Various factors, such as phonon confinement, strain, crystallite size and crystallite size distribution, defects, non-stoichiometry, and anharmonic effects, can lead to the position's shift of the  $E_{g(1)}$  Raman mode of anatase TiO<sub>2</sub> [53]. Within the framework of this study, the main factors that influence the  $E_{g(1)}$  peak in the studied titanium dioxide powders, prepared via sol-gel method, could be attributed to crystallite size, as well as the presence of an adequate amount of rutile TiO<sub>2</sub> phase combined with anatase, such as for N-TiO<sub>2</sub> powder. These are confirmed by the plot presented in Figure S2, as the  $E_{g(1)}$  peak of the Ag@N-doped TiO<sub>2</sub> powder appears at  $146 \text{ cm}^{-1}$ , approximately, contrary to N,S-codoped TiO<sub>2</sub> and N-doped TiO<sub>2</sub> powders, where the peak's position appears to be  $144.46$  and  $143.21 \text{ cm}^{-1}$ , respectively, given the fact that Ag@N-doped TiO<sub>2</sub> possesses the smallest crystallite size ( $1.80 \text{ nm}$ ), as well as no rutile phase. It could be also assumed that as the rutile phase vanishes

(see Table 3 of XRD analysis),  $E_{g(1)}$  mode indicates a blue shift as it is extremely sensitive to anatase content, even in the case of low percentages of anatase (<50%) being present.

Due to the strong intensity of the  $E_{g(1)}$  peak of the Ag@N-doped  $TiO_2$  sample, a magnification of the 350–700  $cm^{-1}$  spectral range is provided (Figure S3). Regarding the N-doped  $TiO_2$  sample, except for the Raman active modes ascribed to the anatase  $TiO_2$  phase,  $E_{g(2)}$  mode of rutile  $TiO_2$  phase is observed at  $\approx 448\text{ cm}^{-1}$ , verifying the XRD data presented in Figure 4 and Table 3.

### 3.1.4. BET Analysis

It is well known that the photocatalytic efficiency of a powder can be influenced by the textural as well as by structural parameters. The obtained plots from the BET method are presented in Figure 7. All the recorded  $N_2$ -sorption plots present a crossover of the sorption (black line) and desorption (red line), indicative of the materials' influence on the measuring procedure [54]. Resultant BET surface area values for such materials are reliable due to their estimation by the early part of the adsorption. It is apparent that all types of chemically modified  $TiO_2$  powders were characterized by type IV isotherms, a typical feature of mesoporous nanomaterials [55]. Both the position and shape shift of the hysteresis loops constitute signs of divergence in the pores' size and volume. Insets of Figure 7a–c display the corresponding pore size distribution of the N-doped, N,S-codoped, and Ag-loaded N-doped  $TiO_2$  powder, as determined from the desorption curve according to the BJH method, respectively. The hysteresis loops displayed by the recorded isotherms are of type H2, implying that the chemically modified  $TiO_2$  powders possess a more convoluted pore structure, developing a continual network. Thus, the BJH porous size distribution plots for N-doped and Ag@N-doped  $TiO_2$  powder are narrow, compared to the N,S-codoped one, revealing that in the latest case, it is possible for a pore blocking with a wider neck size distribution to take place [56].

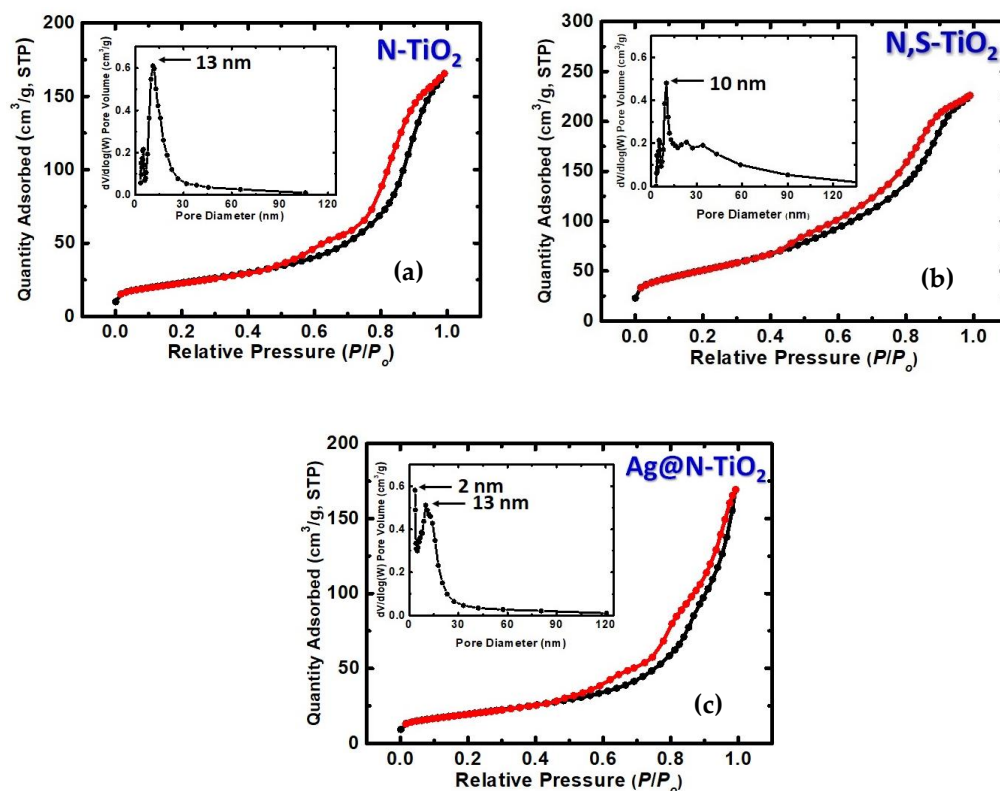


**Figure 7.**  $N_2$ -sorption diagram of: (a) N- $TiO_2$ , (b) N,S- $TiO_2$ , and (c) Ag@N- $TiO_2$  powder, as indicated (sorption: black line and desorption: red line). The insets show the pore size distribution by the BJH method for each chemically modified powder.

The obtained physical parameters such as BET surface area, micropore surface area, cumulative volume, and average pore diameter are summarized in Table 4. Among all synthesized chemically modified TiO<sub>2</sub> powders, the Ag@N-TiO<sub>2</sub> catalyst exhibits the more increased BET surface area and the smallest average pore size, in accordance with the smallest crystalline size as deduced from XRD data (see Table 3).

**Table 4.** Results deduced from BET method. (a) Specific surface area calculated by using Brunauer–Emmett–Teller theory. (b) Micropore surface area via t-plot analysis, according to the Harkins and Jura model. (c) Cumulative volume of pores between 1.7 and 300 nm from N<sub>2</sub>-sorption data and the BJH desorption method. (d) Average pore diameter, calculated by the 4 V/σ method; V was set equal to the maximum volume of N<sub>2</sub> adsorbed along the isotherm as P/P<sub>0</sub> → 1.0.

Sample	BET Surface Area (m <sup>2</sup> g <sup>-1</sup> ) (a)	Micropore Surface Area (m <sup>2</sup> g <sup>-1</sup> ) (b)	Cumulative Volume (1.7–300 nm) (cm <sup>3</sup> g <sup>-1</sup> ) (c)	Average Pore Diameter (nm) (d)
TiO <sub>2</sub> (P25)	~53 [57]	-	0.48 [58]	86 [57]
N-doped TiO <sub>2</sub>	58	3	0.3	13
N,S-codoped TiO <sub>2</sub>	72	4	0.3	15
Ag@N-doped TiO <sub>2</sub>	81	6	0.3	7.7

### 3.1.5. XPS Analysis

For investigating the surface, as well as the chemical state of the elements existing in the synthesized chemically modified TiO<sub>2</sub> powder samples, XPS analysis was conducted. Figure 8 depicts the wide survey spectrum of N-doped TiO<sub>2</sub>, N,S-codoped TiO<sub>2</sub>, and Ag-loaded N-doped TiO<sub>2</sub> samples. All the peaks were anticipated because the applied synthetic procedure was spotted. More specifically, the Ti2p doublet characterized by a spin orbit splitting equal to 5.75 eV, as well as the binding energy of Ti2p<sub>3/2</sub>, is located at 458.8 ± 0.1 eV and corresponds to Ti<sup>4+</sup> in the TiO<sub>2</sub> chemical state (Figure 9a). The O1s peak can be ascribed to lattice oxygen Ti-O in the TiO<sub>2</sub> state, possessing binding energy equivalent to 530.0 ± 0.1 eV and hydroxides and/or adsorbed water on the surface characterized by a binding energy of 531.7 ± 0.1 eV (Figure 9b) [59]. Figure 10 shows the N1s peak centered at 400.1–400.5 eV, approximately, which can be assigned to N-Ti bonds [60]; and given that the observed line is located above 400 eV, an interstitially doped nitrogen mechanism could be proposed [61,62]. Figure 11a,b shows the Ag3d and AgMNN X-ray-induced Auger spectrum from the Ag@N-TiO<sub>2</sub> sample. The modified Auger parameter (α) comprises the sum of the Ag 3d<sub>5/2</sub> photoelectron peak's binding energy, and the Ag M<sub>4</sub>N<sub>45</sub>N<sub>45</sub> Auger peak's kinetic energy is widely utilized to estimate the chemical state of silver atoms, which is found at 722.6 eV (α = 367.1 eV + 355.5 eV) attributed to Ag<sup>+</sup> ions [63]. Lastly, Figure 12 shows the S2p peak of the N,S-TiO<sub>2</sub> sample. The peak consists of two doublets (with spin orbit splitting 1.2 eV) where the binding energy of S2p<sub>3/2</sub> components is centered at 167.7 eV assigned to sulphones (O=S=O) [64], and at 166.9 eV, is assigned to sulphites (SO<sub>3</sub><sup>2-</sup>) [65]. Generally, for S-doped TiO<sub>2</sub> powders, a peak around 168 eV in the S2p spectra is usually ascribed to sulphur on the higher oxidation state (S<sup>4+</sup>, S<sup>6+</sup>), substituting Ti atoms in the TiO<sub>2</sub> lattice [61].

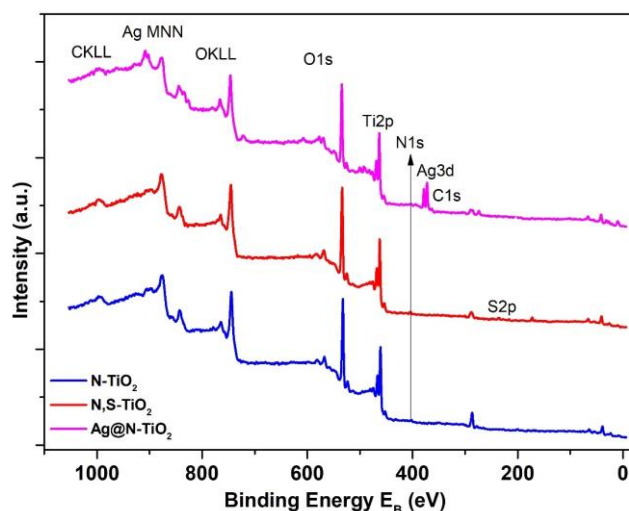


Figure 8. Wide survey XPS spectra of all studied chemically modified TiO<sub>2</sub> powders.

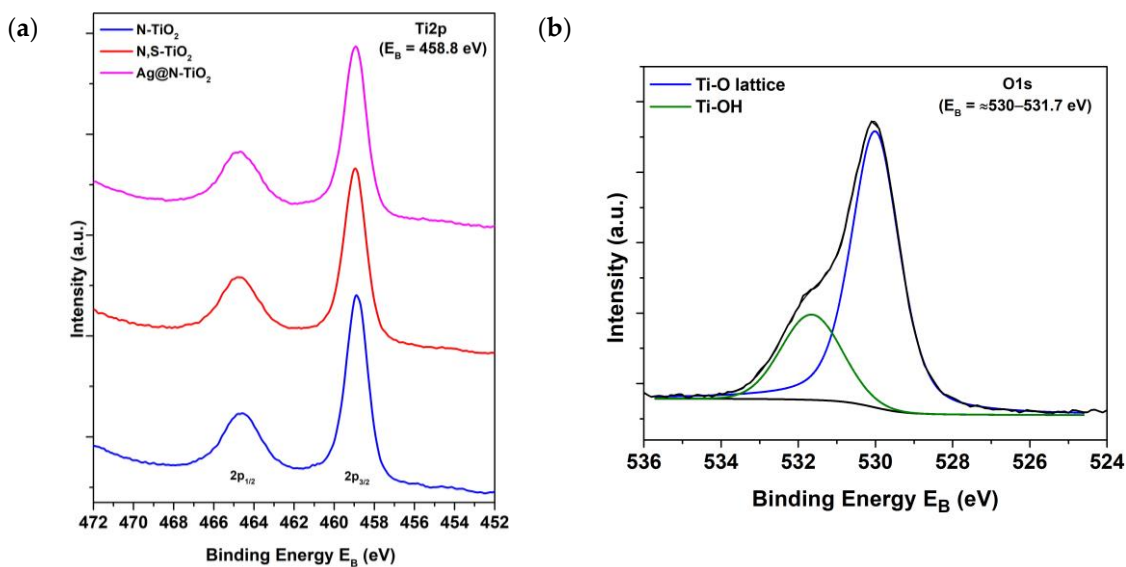


Figure 9. (a) Ti2p XPS peak of N-TiO<sub>2</sub>, N,S-TiO<sub>2</sub>, and Ag@N-TiO<sub>2</sub>. (b) Indicative O1s XPS peak of the studied chemically modified TiO<sub>2</sub> powders.

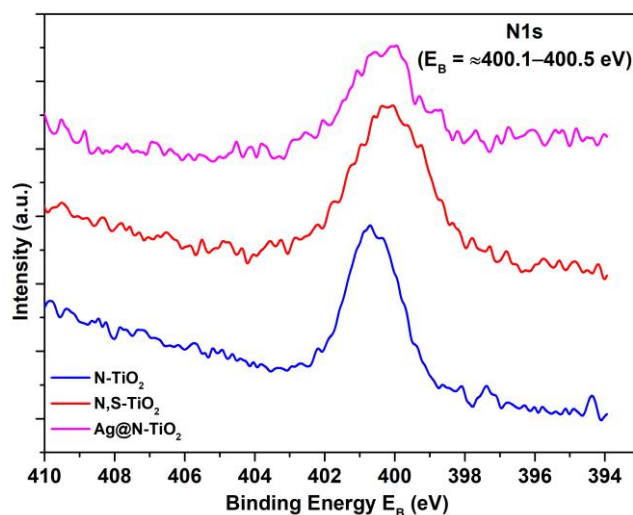


Figure 10. N1s peak of N-TiO<sub>2</sub>, N,S-TiO<sub>2</sub>, and Ag@N-TiO<sub>2</sub> samples.



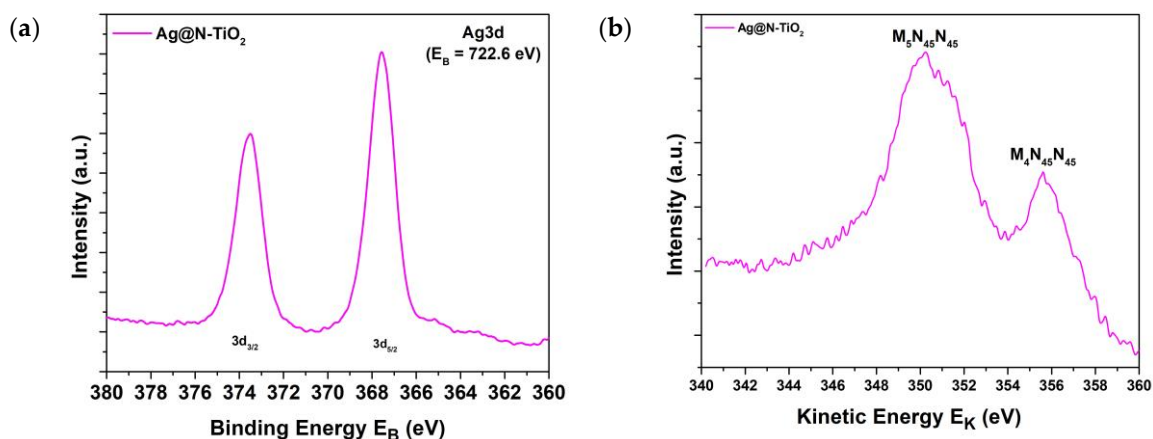


Figure 11. Ag3d peak (a) and XAES detailed region of Ag MNN (b) of the Ag@N-TiO<sub>2</sub> sample.

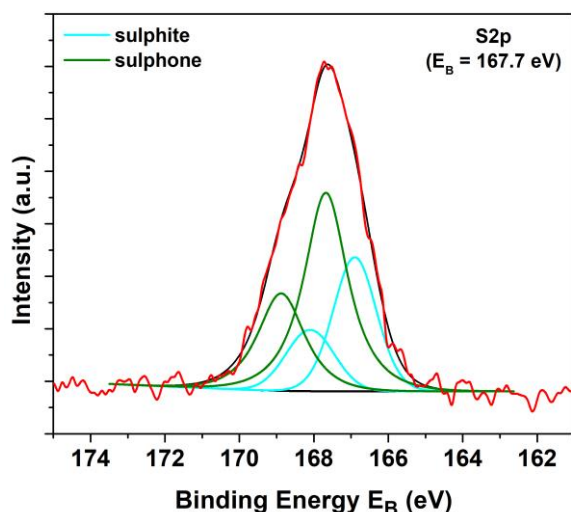


Figure 12. Deconvoluted S2p peak of the N,S-TiO<sub>2</sub> sample.

### 3.1.6. Diffuse Reflectance UV-Vis Spectroscopy Analysis (DRS)

Band gap energy ( $E_g$ ) constitutes a crucial parameter that has to be considered during photocatalytic studies. The DRS of the as-prepared N-TiO<sub>2</sub>, N,S-TiO<sub>2</sub>, and Ag@N-TiO<sub>2</sub> samples along with the spectrum of the commercially available TiO<sub>2</sub> (P25) for comparison are shown in Figure 13a.

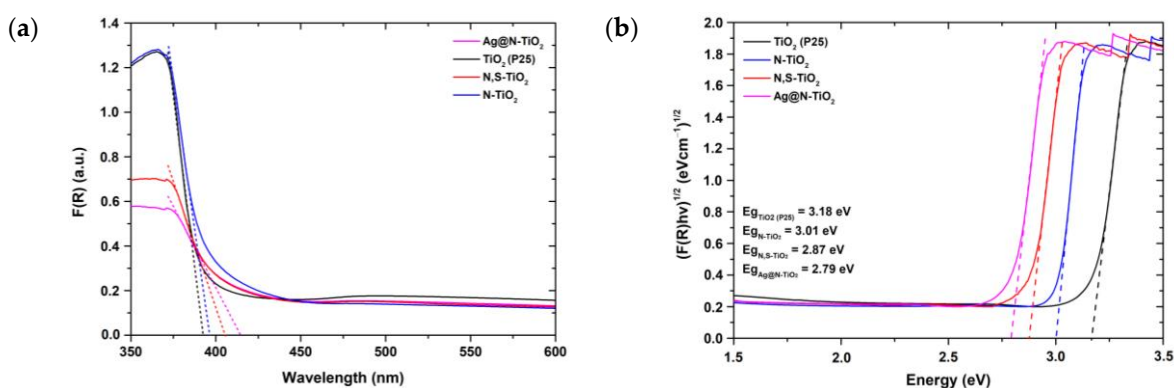


Figure 13. (a)  $F(R)$  reflectance as a function of the wavelength for the TiO<sub>2</sub> powders and (b) energy band gap ( $E_g$ ) of the same samples.

Kubelka–Munk (K–M) method was implemented in order to rate the reflectance (Figure 13a) of the TiO<sub>2</sub> powders via Equation (6) [41]:

$$F(R) = \frac{(1 - R)^2}{2R} \quad (6)$$

where R is the reflectance.

As presented in Figure 13a, it can be observed that the absorption edges of Ag@N-TiO<sub>2</sub>, N,S-TiO<sub>2</sub>, and N-TiO<sub>2</sub> are located at 415, 405, and 396 nm, respectively. All the chemically modified TiO<sub>2</sub> powders showed a broader range of absorption of visible light than TiO<sub>2</sub> P25 (391 nm). However, the Ag@N-TiO<sub>2</sub> sample presented the broadest one.

Figure 13b presents the direct E<sub>g</sub> of the synthesized TiO<sub>2</sub> powders, employing the K–M model vs. energy by extrapolating the linear region of the spectra (F(R)hv)<sup>1/2</sup> vs. hv. Energy band gap (E<sub>g</sub>), which was estimated through Tauc's equation (Equation (7)):

$$ahv = A(hv - E_g)^n \quad (7)$$

where E<sub>g</sub> stands for the energy band gap, h corresponds to Planck's constant, v is the frequency, α represents the absorption coefficient, and n = 1/2 [41].

The band gaps of commercially available TiO<sub>2</sub> (P25), N-TiO<sub>2</sub>, N,S-TiO<sub>2</sub>, and Ag@N-TiO<sub>2</sub> were found equal to 3.18 eV, 3.01 eV, 2.87 eV, and 2.79 eV, respectively. According to the results, Ag-loaded N-doped TiO<sub>2</sub> powder indicated the protracted absorption edge coupled with the lowest band gap energy that constitutes desirable characteristics for the enhancement of its photocatalytic efficiency [66].

### 3.1.7. Dynamic Light Scattering (DLS) Analysis

The DLS measurements were conducted at pH values equal to 6.65 ± 0.01. The hydrodynamic radius distribution vs. scattering light intensity is depicted in Figure S4 for all studied TiO<sub>2</sub> powder samples. In accordance with the obtained results, Ag@N-TiO<sub>2</sub> sample presented an optimal particle size distribution, characterized almost by monodispersity (PDI ≈ 0.1) (see Table 5). The size distribution of all the as-synthesized powders is located between 10 and 100 nm with a maximum value ≈30 nm. N-doped TiO<sub>2</sub> and N,S-codoped TiO<sub>2</sub> are also characterized by a small fragment of few micro-sized (μm) particles, owing likely to the presence of large agglomerates (Figure S4b,c) that correspond to a reduced portion of the scattered light intensity. The results of the DLS measurements are summarized in Table 5 for all chemically modified TiO<sub>2</sub> samples. According to existing literature [67], the average mean size of the commercially available TiO<sub>2</sub> (P25) is ≈240 nm.

**Table 5.** Size distribution results obtained from DLS measurements from dispersion aqueous solutions of chemically modified TiO<sub>2</sub> powders.

Sample	Hydrodynamic Diameter (D <sub>h</sub> ) (nm)	PdI *
N-TiO <sub>2</sub>	29.54 ± 1.57	0.203 ± 0.007
N,S-TiO <sub>2</sub>	28.43 ± 1.23	0.146 ± 0.011
Ag@N-TiO <sub>2</sub>	28.13 ± 1.36	0.117 ± 0.013

Note: \* PdI = Polydispersity Index.

### 3.1.8. FESEM Analysis

The primary morphological aspects of the prepared chemically modified TiO<sub>2</sub> powders observed using a field emission scanning electron microscope (FESEM) are presented in Figure 14.

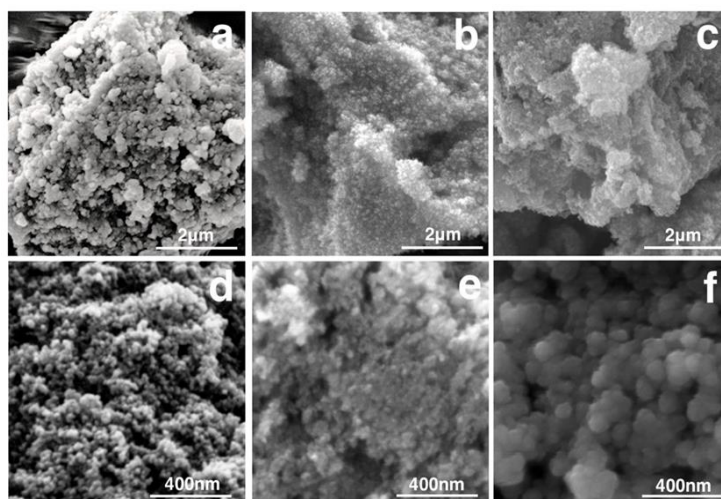


**Figure 14.** FESEM images of N-doped TiO<sub>2</sub> (a,d), N, S-doped TiO<sub>2</sub> (b,e), and Ag@N-doped TiO<sub>2</sub> (c,f) at two magnifications.

Figure 14a–c indicates that the chemically modified TiO<sub>2</sub> particles are spherical-shaped and evenly distributed, whereas Figure 14d–f reveals that the mean diameter of nanoparticles seem to be less than  $\approx 50$  nm, in accordance with the aforementioned XRD and DLS results. In addition, in Figure 14f, it can be observed that Ag@N-doped TiO<sub>2</sub> powder consists of larger and distinct spherical aggregates of nanoparticles compared to N-doped and N,S-doped TiO<sub>2</sub> (see Figure 14d,e, respectively).

### 3.2. Photocatalytic Study of the Chemically Modified TiO<sub>2</sub> Powders

#### 3.2.1. Study of the Photocatalytic Efficiency towards the Degradation of Rhodamine B

The photocatalytic efficiency of the developed chemically modified TiO<sub>2</sub> powder samples was gauged through the degradation of Rhodamine B (RhB) dye aqueous solution upon visible light irradiation. All the photocatalytic tests were carried out at 25 °C and pH values equal to  $6.65 \pm 0.01$ . Figure 15 depicts the photocatalytic effectiveness of all the examined TiO<sub>2</sub> powders. The commercially available TiO<sub>2</sub> (Evonik P25) was also included in the plot as a reference, in order to verify the enhancement of TiO<sub>2</sub>'s photocatalytic efficiency under visible light irradiation through the as-described chemical modifications. Photolysis (RhB photolysis), as well as adsorption-desorption equilibrium (RhB dark), for the same duration as the photocatalytic process, without irradiation (dark condition) and under constant stirring, were additionally conducted. The amount of Rhodamine B degraded under visible light irradiation was calculated less than 1% when imposing irradiation, confirming that the RhB's degradation rate unaccompanied by each studied powder is overly modest. Coherent results emerged from the procedure that took place under a dark state, verifying the dye's stability [68]. Moreover, the real-time UV-visible spectra, recorded every 15 min during the photocatalytic tests, are presented in Figure S5a–c. The data acquired from the recorded real time UV-visible spectra were used, in order to monitor the degradation rate of RhB over time during the study of the powders' photocatalytic efficiency, as well as to verify the mechanism of its degradation. In general, two pathways in which RhB can be degraded exist: (a) N-deethylation and (b) disorder of its conjugated structure. When the first degradation mechanism takes place, a blue shift in the maximum absorption is observed, while during the second mechanism, no blue shift in the absorption maxima is observed, and instead it progressively reduces over time [69]. More specifically, during the former degradation pathway, the maximum shifts from 554 (characteristic peak of RhB) to 498 nm (blue shift); however, the majority of the existing literature asserts the simultaneous contribution of both pathways in RhB degradation [70,71]. The real-time UV-visible spectra acquired for all studied chemically

modified TiO<sub>2</sub> powders during the photocatalytic tests under visible light irradiation (Figure S5a–c) clearly indicate that both pathways are observed, playing a major role towards RhB degradation.

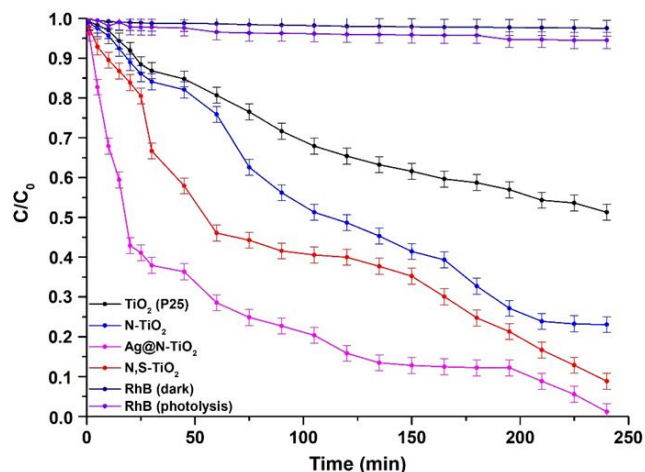


**Figure 15.** Degradation curves of Rhodamine B for the chemically modified TiO<sub>2</sub> powders vs. time under visible light irradiation. The photolysis of RhB and its degradation in the dark are also included.

During the tests, the Ag@N-TiO<sub>2</sub> powder presented the highest efficiency among all studied chemically modified TiO<sub>2</sub> powders, achieving total degradation (100%) of RhB dye at 240 min under visible light irradiation. According to the acquired data (see Figure 15), the chemical modifications of TiO<sub>2</sub> result in an increased photocatalytic degradation of RhB dye, in comparison to the commercially available (un-doped) TiO<sub>2</sub> powder, which indicated a degradation percentage equal to  $48.28 \pm 1.04\%$  within 240 min. This is due to the dopant restraining the recombination of the photo-generated electrons and holes [72,73]. In addition, it was observed that the codoped N,S-TiO<sub>2</sub> powder degraded the dye at a percentage equal to  $92.83 \pm 1.29\%$  after 240 min, while the nitrogen-doped TiO<sub>2</sub> sample achieved a degradation equal to  $74.76 \pm 1.58\%$  at the same time (240 min).

In order to ascertain the results obtained from RhB degradation studies, TOC analysis was also conducted for evaluating RhB's mineralization percentage during the photocatalytic experiments. The percentage of RhB mineralization was estimated using Equation (8):

$$\text{Mineralization} = 1 - \frac{\text{TOC}_{\text{final}}}{\text{TOC}_{\text{initial}}} \times 100\% \quad (8)$$

where TOC<sub>initial</sub> is the total organic carbon concentration in the medium before the photocatalytic study and TOC<sub>final</sub> is the total organic carbon concentration in the medium after the conduction of photocatalysis [74]. The resulted data are represented in Figure S6. According to the results acquired by the TOC analysis, Ag-loaded N-doped TiO<sub>2</sub> powder indicates the highest rate of RhB mineralization under visible light irradiation, thus verifying the observations that aroused from the RhB degradation studies.

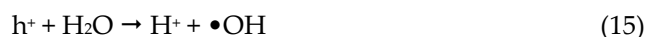
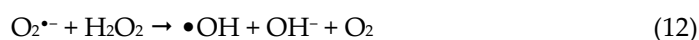
The high photocatalytic performance of the Ag@N-TiO<sub>2</sub> powder in comparison to the other two examined powders can be ascribed to the rather smaller average crystallite size (1.80 nm), lower mean hydrodynamic diameter ( $\approx 28$  nm), enhanced BET surface area ( $81 \text{ m}^2\text{g}^{-1}$ ), as well as the smallest average pore diameter, compared to the other two types of tested TiO<sub>2</sub> powders. The enhancement of the specific surface area leads to a significant increase in the light-harvesting capacity, as well as faster interfacial charge transfer rates, while a sufficiently enhanced contact area among the examined powders and the dye's molecules could be established, leading to a maximum adsorbent effect. This could favor

the availability of an increased number of active sites for the efficient interaction among the Ag@N-TiO<sub>2</sub> and RhB molecules [75].

### 3.2.2. Photocatalytic Mechanism

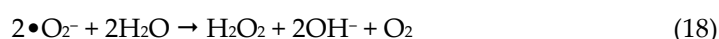
The increased photocatalytic efficiency of the Ag loaded N-doped TiO<sub>2</sub> powder under visible light (VL) irradiation can be assigned to the reciprocal effect of nano-scaled nitrogen and silver particles. Nitrogen's interchange into the TiO<sub>2</sub>'s lattice comprises a more efficient strategy for extending the edge of absorption to the visible light region, because of the induced N2p state. At the same time, interstitial defects, such as interchanged N and/or O vacancies, also enhance the visible response of TiO<sub>2</sub>. Furthermore, the Ag nanoparticles present in the Ag@N-TiO<sub>2</sub> powder sample can compromise effective electron traps, suppressing the electron-hole recombination [76]. Upon irradiation within the visible area of the spectrum, electrons (e<sup>-</sup>) are agitated from the nitrogen impurity energy level to the TiO<sub>2</sub>'s conduction band (CB). As a result, they are engaged by the deposited Ag. Subsequently, they are rapidly moved to the adsorbed O<sub>2</sub> on the surface of TiO<sub>2</sub>, leading to the development of superoxide anion radicals (SAR) (<sup>•</sup>O<sub>2</sub><sup>-</sup>) that can further promote the photocatalytic decomposition of RhB. At the same time, the photogenerated holes (h<sup>+</sup>) of the valence band (VB) react with OH<sup>-</sup>, producing extremely active oxygen species <sup>•</sup>OH. The generated <sup>•</sup>OH and <sup>•</sup>O<sub>2</sub><sup>-</sup> are responsible for the degradation of RhB [66].

In the case of N,S-codoped TiO<sub>2</sub> powder, the insert of nitrogen and sulfur into the lattice of TiO<sub>2</sub> promotes the development of mid-gap energy levels, such as N2p and S2p between the O2p VB and the Ti3d CB [77]. This fact results in the reduction of the TiO<sub>2</sub>'s E<sub>g</sub> and, subsequently, the e<sup>-</sup> are more likely to migrate from the VB of the TiO<sub>2</sub> to its CB under light absorption, leading to the enhanced photocatalytic activity of the N,S-codoped TiO<sub>2</sub>. Additionally, the aforementioned photo-excited e<sup>-</sup> accumulate on the as-synthesized catalyst's surface and are restrained by dissolved and/or atmospheric oxygen, developing extremely oxidative species, such as SAR and <sup>•</sup>OH. The aforementioned radicals are in control of the degradation of RhB. However, the h<sup>+</sup> generated within the VB of the catalyst are restrained by OH<sup>-</sup> ions, producing <sup>•</sup>OH that are also in charge of RhB degradation [78]. In summation, the degradation mechanism of RhB dye through the utilization of N,S-codoped TiO<sub>2</sub> can be described by the following Equations (9)–(16):



As for the N-doped TiO<sub>2</sub>, under VL irradiation, e<sup>-</sup> can be transferred from the N2p energy level to the CB, promoting the generation of e<sup>-</sup> and h<sup>+</sup> in the CB and N2p state, respectively. The photo-induced h<sup>+</sup> in the N2p state can lead to the oxidation of the adsorbed RhB dye on the surface of the catalyst. Simultaneously, the h<sup>+</sup> can serve as oxidizers for the hydroxyl groups that are present on the catalyst's surface, resulting in the development of <sup>•</sup>OH radicals. Given the fact that <sup>•</sup>OH constitute the primary oxidant during photo-oxidation reactions, they possess a crucial effectiveness in the oxidation of RhB. As a result, the existence of more <sup>•</sup>OH achieves enhanced photocatalytic performance [79]. The photo-excited electrons can be trapped by oxygen surficially adsorbed on the catalyst,

producing superoxide anion radicals ( $\bullet\text{O}_2^-$ ) that play a vital role in the photocatalytic oxidation of RhB (see Equation (17)). However, these radicals can react with adsorbed water and promote the generation of  $\text{H}_2\text{O}_2$  (see Equation (18)) and then the production of  $\bullet\text{OH}$  (see Equation (19)) [80]. It is generally accepted that SAR are less active than  $\bullet\text{OH}$  for the oxidation of dyes under VL irradiation [79]. Therefore, the photocatalytic efficiency of N-doped  $\text{TiO}_2$  towards the oxidation of Rhodamine B depends on the rate of  $\bullet\text{OH}$  production. The presence of oxygen apart from promoting the development of  $\bullet\text{OH}$  and SAR also leads to the prevention of photo-generated charges recombination; thus, causing a significant increase in the photocatalytic activity of the N-doped  $\text{TiO}_2$  catalyst.



### Hydroxyl Radical-Scavenging Photocatalytic Study

Based on current literature, among the ROS that account for the bactericidal activity of  $\text{TiO}_2$  photocatalysts towards *E. coli* bacteria,  $\bullet\text{OH}$  radicals constitute the prevailing oxidative species [81,82].

According to the previously mentioned photocatalytic mechanism of the synthesized chemically modified  $\text{TiO}_2$  powders,  $\text{H}_2\text{O}_2$  may be formed during the photocatalytic process (see Equation (11)) through its reaction with conduction band electrons ( $e^-$  acceptor) and afterwards be degraded to radicals, including  $\bullet\text{OH}$  (see Equations (13) and (19)).

Direct photolysis of the produced  $\text{H}_2\text{O}_2$  could also take place, provoking the yield of  $\bullet\text{OH}$  [83]. Despite this, the generation rate of  $\bullet\text{OH}$  radicals from such pathway is rather modest in the visible light region, in which the photocatalytic bacteria inactivation is examined within the present study, due to its low molar extinction coefficient [83].

Previous reports have indicated that  $\text{H}_2\text{O}_2$  and light irradiation may operate synergistically in bacteria cell membranes' hampering, thus rendering bacteria more prone to oxidative inactivation [84,85]. It is generally accepted that cell membranes constitute the decisive part of the bacteria to be assaulted for their effective inactivation [83]. It has been suggested that the cell membrane is initially harmed, ensued by a gradual damage of the cytoplasmic membrane and intracellular components [86,87]. The produced  $\bullet\text{OH}$  radicals attack the polyunsaturated phospholipid components of the lipid membrane, thus causing significant disorder in the cell membrane. The oxidation of the lipid membrane leads to a loss of key cell functions, which depend on the coherence of the cell membrane, like respiration, eventually inducing cell death (Figure S7) [83].

For confirming the  $\bullet\text{OH}$  radicals' generation and, as a result, the production of  $\text{H}_2\text{O}_2$  during the photocatalytic procedure, as well as the bactericidal efficiency of the as-synthesized  $\text{TiO}_2$  powders, an alcohol, and especially n-butanol, was utilized as scavenging factor. The selection of n-butanol was based on existing research findings, proving that the proposed alcohol presents enhanced reactivity with  $\bullet\text{OH}$  radicals and negligible influence on  $\text{H}_2\text{O}_2$  evolution, assuring that the produced  $\bullet\text{OH}$  radicals, and subsequently  $\text{H}_2\text{O}_2$ , can be attributed to the previously mentioned photocatalytic mechanism [88].

Figure S8 presents the effect of the  $\bullet\text{OH}$  radical scavenger on RhB photocatalytic degradation of the studied  $\text{TiO}_2$  nanopowders in relation to degradation in absence of a scavenger, after 60 min visible light irradiation. Normalized RhB degradation percentages are demonstrated in Figure 16. A normalized RhB degradation occurs with the presence of each studied catalyst and in the absence of the scavenger, and thus is always equal to 100% [89].

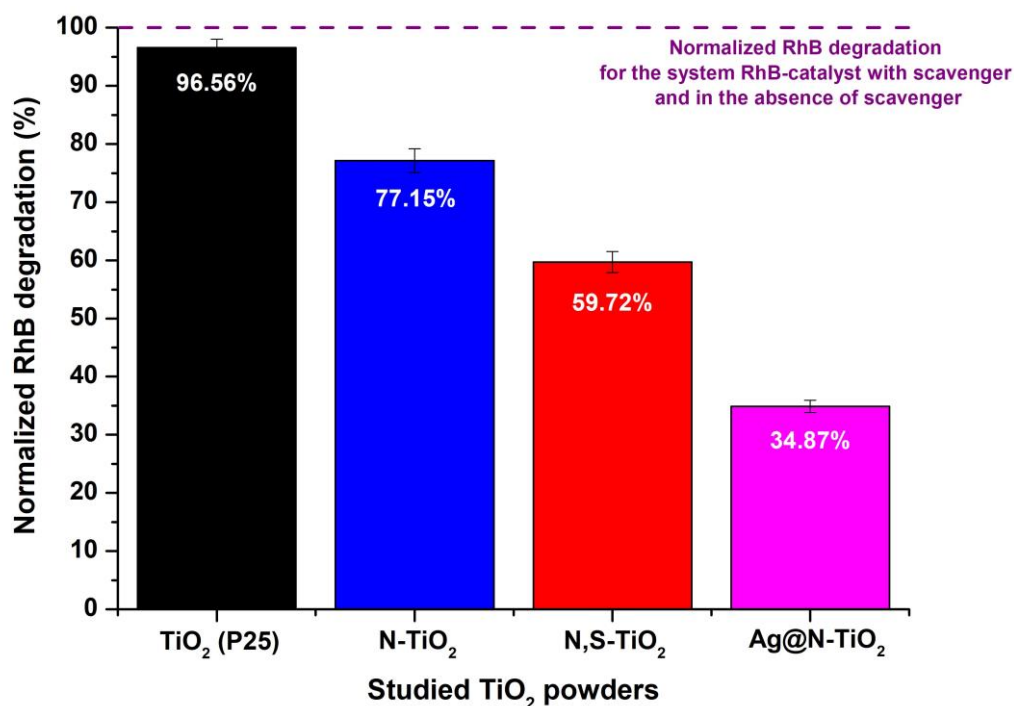


Figure 16. Normalized RhB degradation on examined TiO<sub>2</sub> powders.

For all studied chemically modified TiO<sub>2</sub> powders, a photocatalytic activity reduction is observed after adding n-butanol. The observed results reveal that the •OH radicals are produced during the photocatalytic study trials. Among all examined powders, Ag@N-TiO<sub>2</sub> indicated the greatest reduction in its photocatalytic activity (Figure 16), implying the most increased production of •OH radical and simultaneously the generation of H<sub>2</sub>O<sub>2</sub> during the photocatalytic experiments.

### 3.2.3. Photocatalytic Kinetic Model Study

Figure S9 presents the results of the kinetic model studies under VL irradiation, as a variation of  $-\ln(C/C_0)$  vs. time for the examined chemically modified TiO<sub>2</sub> powders. The rate of the photocatalytic absorption of RhB onto the studied powders' surface is relatively faster for the Ag@N-TiO<sub>2</sub>, based on the pseudo-first order kinetics ( $0.166 \text{ min}^{-1}$ ), compared to the other two samples that are described by the following equation (Equation (20)) [68]:

$$-\ln\left(\frac{C}{C_0}\right) = kt \quad (20)$$

where  $C_0$  and  $C$  are the initial and reaction time concentrations of RhB dye, respectively,  $k$  represents the apparent rate constant of the photocatalytic oxidation, and  $t$  corresponds to the irradiation time. The slope of the linear fitted plot corresponds to the apparent rate constants of the examined chemically modified TiO<sub>2</sub> powders (see Table 6).

Table 6. Kinetic parameters of the studied TiO<sub>2</sub> powders under visible light photocatalysis.

Sample Name	Pseudo-First-Order Kinetic Model		Pseudo-Second-Order Kinetic Model	
	$k_1$ ( $\text{min}^{-1}$ )	$R^2$	$k_2$ ( $\text{g}\cdot\text{mg}^{-1}\cdot\text{min}^{-1}$ )	$R^2$
N-doped TiO <sub>2</sub>	0.009	0.838	0.474	0.740
N,S-codoped TiO <sub>2</sub>	0.036	0.935	0.537	0.888
Ag@N-doped TiO <sub>2</sub>	0.166	0.981	0.567	0.681



The kinetics of photocatalytic experiments may be ascribed also by the pseudo-second-order equation that is described below (Equation (21)) [68]:

$$\frac{t}{q_t} = \frac{1}{k_2 q_e^2} + \frac{1}{q_e} t \quad (21)$$

where  $q_t$  and  $q_e$  correspond to the pollutant amount adsorbed at time  $t$  and equilibrium, respectively (mg/g), while  $k_2$  is the rate constant ( $\text{g}\cdot\text{mg}^{-1}\cdot\text{min}^{-1}$ ). Compared to pseudo-first-order kinetics (see Figure S9), the  $R^2$  values of the pseudo-second-order kinetic study (Figure S10) are found to be quite poor. Table 6 presents the kinetic parameters of the chemically modified  $\text{TiO}_2$  powders.

Considering, therefore, the  $R^2$  values of the kinetic studies, the photocatalytic oxidation of RhB dye under VL irradiation for all chemically modified titania particles follows pseudo-first-order reaction kinetics (Figure S9).

### 3.3. Reusability Studies

Photostability, as well as catalyst lifetime, compromise crucial economic parameters in the photocatalytic procedure [90]. The reusability experiments were also conducted under VL irradiation, with the loading of the catalyst equal to 5 mg,  $\text{pH} = 6.65 \pm 0.01$  and  $10 \text{ mgL}^{-1}$  RhB initial concentration. After each experimental run (VL irradiation for 240 min), the catalyst (each examined chemically modified  $\text{TiO}_2$  powder) RhB dye solution was centrifuged at 9000 rpm for 10 min. Each studied powder was rinsed thrice with distilled water, heated at  $70^\circ\text{C}$  for 24 h, and recovered and reused without any further treatment [91]. The procedure took place five times (five cycles) and the results are demonstrated in Figures S11a–c and 17.

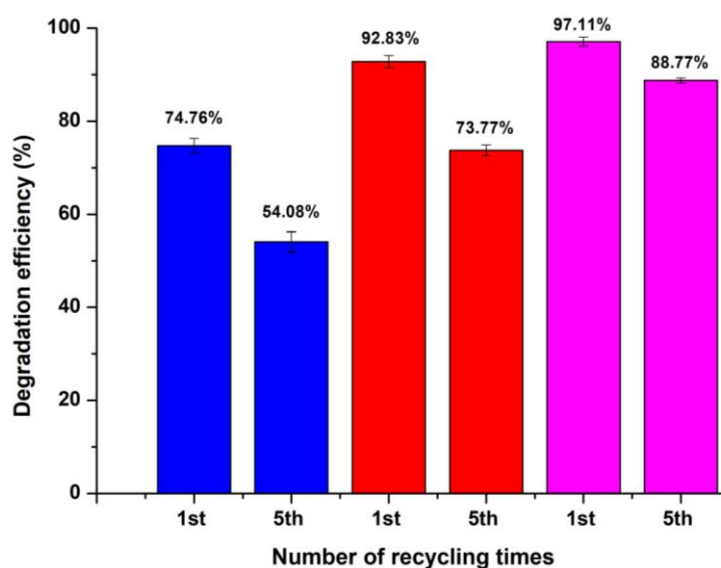


**Figure 17.** Recycling activity of the studied chemically modified  $\text{TiO}_2$  powders after 5 experimental photocatalytic cycles (N-doped  $\text{TiO}_2$  in blue, N,S-codoped  $\text{TiO}_2$  in red, and Ag-loaded N-doped  $\text{TiO}_2$  in purple).

As presented in Figure 17, the degradation efficiency of the N- $\text{TiO}_2$  sample decreased from  $74.76 \pm 1.58\%$  at the first cycle to  $54.08 \pm 2.12\%$  after five cycles. In the case of N,S- $\text{TiO}_2$ , the efficiency of the RhB degradation declined from  $92.83 \pm 1.29\%$  to  $73.77 \pm 1.14\%$  after five cycles. The observed reduction in the degradation efficiency's rate of the N-doped  $\text{TiO}_2$  catalyst after the five degradation cycles may be attributed to the adsorption of incompletely photo-degraded products on its surface [92]. On the other hand, the Ag-loaded N-doped  $\text{TiO}_2$  sample did not indicate a significant loss of efficiency ( $8.34\% \pm$

0.55%) after five cycles of the photocatalytic degradation procedure. Furthermore, the stability of the chemically modified TiO<sub>2</sub> powders was verified after the five experimental cycles using XRD (see Figure S12). It was observed that all the studied TiO<sub>2</sub> powders presented negligible crystalline phase alterations, only an infinitesimal amplification on the peaks' intensity. Such behavior implies that there was no change in the photocatalysts' structure after RhB degradation experiments or exposure to air, thus indicating their good photochemical stability, while a slight intensity increase could be possibly related to an enhancement of the crystallites' dimensions, due to the photoirradiation activation process [93].

#### 3.4. Silver Dissolution Study of the Ag@N-TiO<sub>2</sub> Powder

Water salinity has been reported to lead to significant silver leaching [94]. In the present study, in order to estimate the potential silver leaching of the Ag-loaded N-doped TiO<sub>2</sub> powder, a certain amount of Ag@N-TiO<sub>2</sub> powder was added in 0.09 M aqueous solution of NaCl (99.8%, Lach-Ner, Czech Republic). All the experiments were conducted under dark and continuous stirring, at room temperature. At certain time points (every 15 min), the amount of the Ag@N-TiO<sub>2</sub> powder was separated from the NaCl solution via centrifugation at 9000 rpm for 10 min and the silver concentration in the solution was measured by ICP-MS (see Figure S13). The extracted powder was rinsed with water, dried and, then transferred into a new solution. In distilled water, the concentration of Ag deriving from Ag@N-TiO<sub>2</sub> powder was <0.02 µmol/L, while a rate less than 0.17% of Ag leached out during the experimental procedure (240 min), verifying the poor dissolution efficiency of silver in distilled water [95].

The concentration of silver ion dissolved from Ag-loaded N-doped TiO<sub>2</sub> powder declined nearly linearly in the first 180 min, as shown in Figure S13. Then, the silver concentration in the solution exhibited a constant value of ≈0.09 µmol/L.

#### 3.5. Photocatalytic Disinfection Results on Real MWTP Samples

Given the fact that the main goal of this study was to examine the ability of the proposed photocatalytic system towards the substitution of the chlorination/dechlorination step and overcoming its undesirable and harmful byproducts, the effluents were treated after the Step D. The effluents were added inside the photocatalytic tank in the presence of N-doped TiO<sub>2</sub>, N,S-doped TiO<sub>2</sub>, Ag@N-doped TiO<sub>2</sub>, or TiO<sub>2</sub> (P25) powder and the irradiation of the samples was performed for 5, 10, 15, 20, 25, 30, 35, and 40 min, respectively. The EC and CF experiments were performed in triplicate and the concentration of bacteria in the treated water, as collected from the precipitation tank, was determined using the EC and CF tests. The initial concentration in the EC and CF experiments was  $14.1 \times 10^6$  CFU/mL and  $40 \times 10^6$  CFU/mL, respectively. The effluent samples were also irradiated with light without the presence of the studied chemically modified powders. No significant alteration in the effluents' concentration of bacteria was observed. The results of the photocatalytic experiments are shown in Figures 18 and 19.

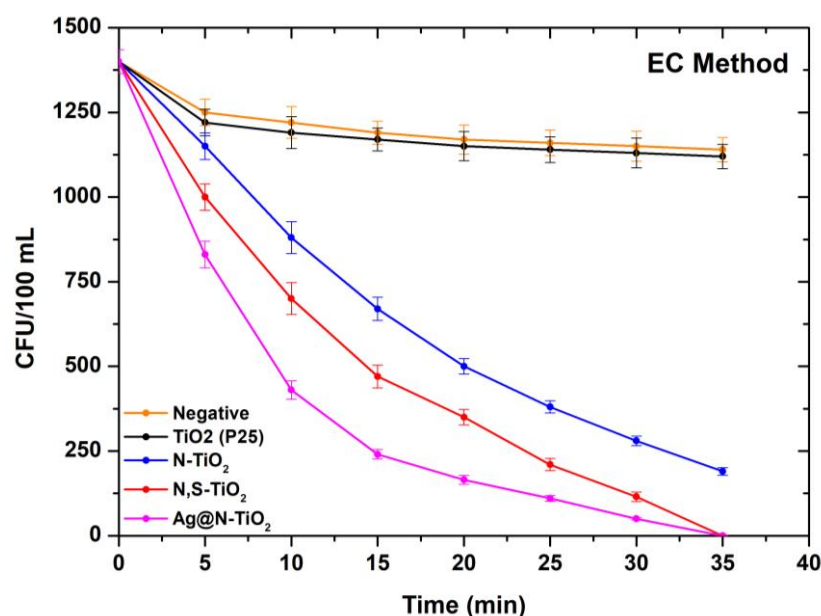


**Figure 18.** Concentration of bacteria (CFU/100 mL) vs. the duration of the photocatalytic disinfection step (EC test).

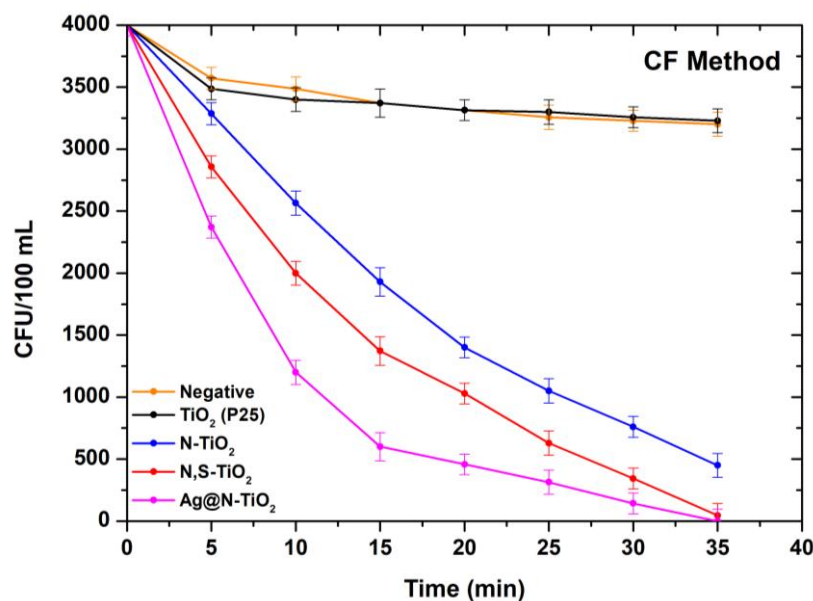


**Figure 19.** Concentration of bacteria (CFU/100 mL) vs. the duration of the photocatalytic disinfection step (CF test).

The photocatalytic tests demonstrated that N,S-doped TiO<sub>2</sub> and Ag-loaded N-doped TiO<sub>2</sub> led to complete inactivation of the bacterial population in less than 35 min. This reduction is perhaps associated with the antimicrobial properties of Ag that are present in the Ag-loaded N-doped TiO<sub>2</sub> particles.

Additionally, the reusability of the chemically modified TiO<sub>2</sub> powders was assessed and the results are shown in Table 7. Through the evaluation of the aforementioned experimental results, it can be inferred that the proposed chemically modified TiO<sub>2</sub> powders do not present a notable loss of their activity after five consecutive reusability cycles, thus confirming their adequacy to be utilized for the proposed application. Among the tested powders, Ag-loaded N-doped TiO<sub>2</sub> powder presented the most satisfying results.

Table 7. Stability tests.

Cycle	CFU after 35 min of Photocatalysis					
	CFU for EC Method			CFU for FC Method		
	N-TiO <sub>2</sub>	N,S-TiO <sub>2</sub>	Ag@N-TiO <sub>2</sub>	N-TiO <sub>2</sub>	N,S-TiO <sub>2</sub>	Ag@N-TiO <sub>2</sub>
1st	70	10	0	150	10	0
2nd	85	8	0	155	20	0
3rd	90	15	0	165	17	1
4th	80	10	2	170	18	2
5th	85	7	0	170	15	0

#### 4. Discussion and Concluding Remarks

Disinfection comprises a rather challenging aspect of wastewater treatment, because of the fast increment of health standards and the constantly raising concerns for pollutant-free water resources. The most ordinarily utilized disinfection methods include the usage of cheap chemicals like chlorine and its products; however, those methods are described by a significant number of grievous drawbacks, such as the generation of chlorinated organic products, which are perilous both for humans and the environment in general, since they are noxious, carcinogenic, and even mutagenic. Furthermore, they are not always able to utterly inactivate all the pathogenic microorganisms potentially present in wastewater effluents on account of their lessened oxidative activity. Given the aforementioned disadvantages, alternative methods for wastewater disinfection are assiduously investigated. Among these alternative disinfection techniques lies photocatalysis utilizing TiO<sub>2</sub> as a catalyst.

TiO<sub>2</sub>-based photocatalysis appears to be an effective water disinfection method with the type of the catalyst's dopant playing a vital role in terms of photocatalytic efficiency and bacterial disinfection. In the framework of this study, different dopants were used to chemically modify TiO<sub>2</sub>, as well as broaden its photocatalytic activation within the visible light region, via a facile sol-gel method, thus resulting in the synthesis of N-doped, N,S-codoped, and Ag@N-doped TiO<sub>2</sub> powders. The successful chemical modification of TiO<sub>2</sub> using N, S, and Ag elements was confirmed by the XPS analysis of the powders' surface. The dominant crystal phase of the chemically modified TiO<sub>2</sub> powders was anatase, with decreased E<sub>g</sub> values compared to commercially available TiO<sub>2</sub> (Evonik P25). The average crystallite size of the as-prepared powders was ranging from 1.80 to 2.13 nm.

The produced powders were initially examined regarding their photocatalytic efficiency towards degradation of RhB dye aqueous solution under visible light irradiation. Ag@N-TiO<sub>2</sub> powder indicated the highest efficiency among all studied chemically modified TiO<sub>2</sub> powders, reaching total degradation (100%) of RhB at 240 min, which was also verified through the results obtained from the TOC analysis. In order to evaluate the durability of the synthesized powders, five recycling trials were conducted, indicating that the photocatalytic efficiency's loss was equal to 20.68%, 19.06%, and 8.34% for N-doped TiO<sub>2</sub>, N,S-codoped TiO<sub>2</sub>, and Ag loaded N-doped TiO<sub>2</sub> powder, respectively.

It is known that reactive oxygen species (ROS) produced during TiO<sub>2</sub> photocatalysis are responsible for the potentially observed bactericidal activity. Among them, H<sub>2</sub>O<sub>2</sub> has been found to lead to the attenuation of cell membranes and subsequent damage of both their cytoplasmic membrane and intracellular components, thus rendering bacteria more prone to oxidative inactivation.

According to the authors' best knowledge, there is no direct method for controlling the production of H<sub>2</sub>O<sub>2</sub> during the photocatalytic procedure, and considering that H<sub>2</sub>O<sub>2</sub> constitutes a •OH precursor, a hydroxyl radical-scavenging photocatalytic process was also conducted for all synthesized powders, using an alcohol, and especially n-butanol, as a scavenger. Based on existing literature, alcohols alone are very unlikely to favor the production of H<sub>2</sub>O<sub>2</sub>, thus ensuring that the observed •OH production was attributed to the proposed TiO<sub>2</sub> photocatalytic mechanism. The obtained results indicated that during the

photocatalytic study, by using n-butanol as a scavenger, Ag@N-TiO<sub>2</sub> presented the highest •OH production among all examined powders. Those results are in line with those that derived from the photocatalytic disinfection trials on the WWTP effluents under visible light irradiation using EC and CF tests. N,S-TiO<sub>2</sub> and Ag@N-TiO<sub>2</sub> powders led to complete bacteria inactivation in less than 35 min, while subsequent stability tests indicated that they did not present a noteworthy reduction in their disinfection efficiency after five re-usability cycles.

The ultimate goal was to propose the powder presenting the optimum properties for replacing the chlorination/dechlorination step (Step E) in an existing WWTP on Antiparos Island, which is characterized by an increased volume of incoming wastewater, especially during the summer period, due to a large number of tourists visiting the island.

As a result, taking into consideration all the obtained experimental data, Ag-loaded N-doped TiO<sub>2</sub> (Ag@N-TiO<sub>2</sub>) powder constitutes a promising candidate for being utilized as a viable, eco-friendly approach for the photocatalytic pathogenic bacteria inactivation application for an alternative disinfection approach for municipal wastewater treatment plant effluents with intense seasonal fluctuations. Therefore, the addition of photocatalytic systems to the existing MWTP infrastructure could anticipate the increase in capacity during the summer period to overcome the necessity to build a new MWTP settlement.

**Supplementary Materials:** The following supporting information can be downloaded at: <https://www.mdpi.com/article/10.3390/w15112052/s1>, Figure S1: Example of a conventional treatment process in a typical municipal WWTP. Specific unit processes may vary in different MWTPs; Figure S2: Magnification of E<sub>g(1)</sub> Raman active mode of anatase TiO<sub>2</sub> phase of the examined chemically modified powders; Figure S3: Magnification of 350–700 cm<sup>-1</sup> Raman spectral region of the studied powders. Anatase TiO<sub>2</sub> modes are marked with black, while rutile TiO<sub>2</sub> modes are marked with orange; Figure S4: Size distribution diagram of the aqueous dispersion solutions of: (a) Ag@N-TiO<sub>2</sub>, (b) N-TiO<sub>2</sub> and (c) N,S-TiO<sub>2</sub> particles; Figure S5: Real time UV-visible spectra obtained every 15 min under visible light photocatalytic degradation of Rhodamine B in presence of: (a) N-doped TiO<sub>2</sub>, (b) N,S-codoped TiO<sub>2</sub> and (c) Ag loaded N-doped TiO<sub>2</sub> powder; Figure S6: Mineralization (%) of each studied chemically modified TiO<sub>2</sub> sample, obtained through TOC analysis, after the photocatalytic procedure under visible light irradiation; Figure S7: Schematic representation of the photocatalytic disinfection of MWTP effluents containing bacteria using the studied chemically modified TiO<sub>2</sub> powders; Figure S8: Study of the photocatalytic efficiency of TiO<sub>2</sub> (P25), N-doped TiO<sub>2</sub>, N,S-codoped TiO<sub>2</sub> and Ag loaded N-doped TiO<sub>2</sub> powders towards the degradation of RhB dye under visible light irradiation in the presence (dashed line) and in the absence (solid line) of n-butanol •OH scavenger; Figure S9: Photocatalytic kinetic model studies for the examined TiO<sub>2</sub> powders following a pseudo-first order model upon visible light irradiation photocatalysis; Figure S10: Photocatalytic kinetic model studies for the examined TiO<sub>2</sub> powders following a pseudo-second order model upon visible light irradiation photocatalysis; Figure S11: Study of the photocatalytic stability of (a) N-doped TiO<sub>2</sub>, (b) N,S-codoped TiO<sub>2</sub> and (c) Ag loaded N-doped TiO<sub>2</sub> powders towards the degradation of RhB dye after 5 cycles under visible light irradiation; Figure S12: XRD patterns of the studied TiO<sub>2</sub> powders after five photocatalytic cycles of RhB degradation under visible light irradiation; Figure S13: Silver dissolution study for the Ag loaded N-doped TiO<sub>2</sub> powder; Table S1: d-spacing calculations for commercial TiO<sub>2</sub> (P25) powder; Table S2: d-spacing calculations for N-doped TiO<sub>2</sub> powder; Table S3: d-spacing calculations for N,S-codoped TiO<sub>2</sub> powder; Table S4: d-spacing calculations for Ag@N-doped TiO<sub>2</sub> powder.

**Author Contributions:** Conceptualization, E.A.P.; formal analysis, D.S.T., M.-A.G. and N.L.; funding acquisition, E.A.P. and P.F.; investigation, D.S.T., M.-A.G. and N.L.; methodology, E.A.P.; project administration, E.A.P.; resources, E.A.P.; supervision, E.A.P.; validation, D.S.T., M.-A.G., N.L., D.C.C., P.F. and E.A.P.; visualization, D.S.T., M.-A.G. and N.L.; writing—original draft, D.S.T., M.-A.G., N.L., L.S., D.C.C. and E.A.P.; writing—review and editing, D.C.C., P.F. and E.A.P. All authors have read and agreed to the published version of the manuscript.

**Funding:** E.A. Pavlatou and D.S. Tsoukleris acknowledge the financial support of European Union's for SELF-CLEAN "Novel Self-cleaning, anti-bacterial coatings, preventing disease transmission on every day touched surfaces", FP7—SME 2012-1 (Research for SMEs) program under grant agreement No 314988. P. Falaras acknowledges funding from Prince Sultan Bin Abdulaziz International

Prize for Water-Alternative Water Resources Prize 2014. D.C Christodouleas acknowledge funding from Greek Diaspora fellowship program of Stavros Niarchos Foundation.

**Data Availability Statement:** Not applicable.

**Acknowledgments:** The authors would like to thank Dionysios D. Dionysiou from the Department of Chemical and Environmental Engineering, University of Cincinnati, United States, for useful discussions and suggestions during manuscript preparation. In addition, the authors would like to thank Henrik E. Fallesen, Daniel Minzari, Claus Barholm-Hansen, and Anette Alsted Rasmussen at IPU Materials for providing FESEM images of the powders, as well as A. Faroupos, Mayor of the Municipality of Antiparos, Greece for providing access to the Wastewater Treatment Plant of Antiparos. The authors would also like to acknowledge Patrina Paraskevopoulou for her assistance with the BET measurements performed in the Department of Chemistry at the National and Kapodistrian University of Athens (NKUA).

**Conflicts of Interest:** The authors declare no conflict of interest.

## References

- Jones, E.R.; van Vliet, M.T.H.; Qadir, M.; Bierkens, M.F.P. Country-level and gridded estimates of wastewater production, collection, treatment and reuse. *Earth Syst. Sci. Data Discuss* **2021**, *13*, 237–254. <https://doi.org/10.5194/essd-13-237-2021>.
- Hube, S.; Wu, B. Mitigation of emerging pollutants and pathogens in decentralized wastewater treatment processes: A review. *Sci. Total Environ.* **2021**, *779*, 146545. <https://doi.org/10.1016/j.scitotenv.2021.146545>.
- Esteban García, B.; Rivas, G.; Arzate, S.; Sánchez Pérez, J.A. Wild bacteria inactivation in WWTP secondary effluents by solar photo-fenton at neutral pH in raceway pond reactors. *Catal. Today* **2018**, *313*, 72–78. <https://doi.org/10.1016/j.cattod.2017.10.031>.
- Symonds, E.M.; Breitbart, M. Affordable enteric virus detection techniques are needed to support changing paradigms in water quality management. *CLEAN—Soil Air Water* **2015**, *43*, 8–12. <https://doi.org/10.1002/clen.201400235>.
- Jabbar, Z.H.; Ebrahim, S.E. Recent advances in nano-semiconductors photocatalysis for degrading organic contaminants and microbial disinfection in wastewater: A comprehensive review. *Environ. Nanotechnol. Monit. Manag.* **2022**, *17*, 100666. <https://doi.org/10.1016/j.enmm.2022.100666>.
- Pasini, S.M.; Valério, A.; Yin, G.; Wang, J.; Guelli Ulson de Souza, S.M.A.; Hotza, D.; Ulson de Souza, A.A. An overview on nanostructured TiO<sub>2</sub>-containing fibers for photocatalytic degradation of organic pollutants in wastewater treatment. *J. Water Process Eng.* **2021**, *40*, 101827. <https://doi.org/10.1016/j.jwpe.2020.101827>.
- Rueda-Marquez, J.J.; Levchuk, I.; Fernández Ibañez, P.; Sillanpää, M. A critical review on application of photocatalysis for toxicity reduction of real wastewaters. *J. Cleaner Prod.* **2020**, *258*, 120694. <https://doi.org/10.1016/j.jclepro.2020.120694>.
- Das, A.; Adak, M.K.; Mahata, N.; Biswas, B. Wastewater treatment with the advent of TiO<sub>2</sub> endowed photocatalysts and their reaction kinetics with scavenger effect. *J. Mol. Liq.* **2021**, *338*, 116479. <https://doi.org/10.1016/j.molliq.2021.116479>.
- Burch, K.D.; Han, B.; Pichtel, J.; Zubkov, T. Removal efficiency of commonly prescribed antibiotics via tertiary wastewater treatment. *Environ Sci Pollut Res.* **2019**, *26*, 6301–6310. <https://doi.org/10.1007/s11356-019-04170-w>.
- Dimapilis, E.A.S.; Hsu, C.S.; Mendoza, R.M.O.; Lu, M.C. Zinc oxide nanoparticles for water disinfection. *Sustain. Environ. Res.* **2018**, *28*, 47–56. <https://doi.org/10.1016/j.serj.2017.10.001>.
- Kozari, A.; Paloglou, A.; Voutsas, D. Formation potential of emerging disinfection by-products during ozonation and chlorination of sewage effluents. *Sci. Total Environ.* **2020**, *700*, 134449. <https://doi.org/10.1016/j.scitotenv.2019.134449>.
- Collivignarelli, M.C.; Abbà, A.; Benigna, I.; Sorlini, S.; Torretta, V. Overview of the main disinfection processes for wastewater and drinking water treatment plants. *Sustainability* **2018**, *10*, 86. <https://doi.org/10.3390/su10010086>.
- Gomes, J.; Matos, A.; Gmurek, M.; Quinta-Ferreira, R.M.; Martins, R.C. Ozone and photocatalytic processes for pathogens removal from water: A review. *Catalysts* **2019**, *9*, 46. <https://doi.org/10.3390/catal9010046>.
- Metcalf, L.; Eddy, H.P.; Tchobanoglous, G. *Wastewater Engineering Treatment Disposal and Reuse*; McGraw-Hill: New York, NY, USA, 1991.
- Huang, H.; Wu, Q.-Y.; Yang, Y.; Hu, H.-Y. Effect of chlorination on endotoxin activities in secondary sewage effluent and typical Gram-negative bacteria. *Water Res.* **2011**, *45*, 4751–4757. <https://doi.org/10.1016/j.watres.2011.06.013>.
- Magaña-López, R.; Zaragoza-Sánchez, P.I.; Jiménez-Cisneros, B.E.; Chávez-Mejía, A.C. The Use of TiO<sub>2</sub> as a Disinfectant in Water Sanitation Applications. *Water* **2021**, *13*, 1641. <https://doi.org/10.3390/w13121641>.
- Hijnen, W.A.M.; Beerendonk, E.F.; Medema, G.J. Inactivation credit of UV radiation for viruses, bacteria and protozoan (oo)cysts in water: A review. *Water Res.* **2006**, *40*, 3–22. <https://doi.org/10.1016/j.watres.2005.10.030>.
- Iakovides, I.C.; Michael-Kordatou, I.; Moreira, N.F.F.; Ribeiro, A.R.; Fernandes, T.; Pereira, M.F.R.; Nunes, O.C.; Manaia, C.M.; Silva, A.M.T.; Fatta-Kassinos, D. Continuous ozonation of urban wastewater: Removal of antibiotics, antibiotic-resistant *Escherichia coli* and antibiotic resistance genes and phytotoxicity. *Water Res.* **2019**, *159*, 333–347. <https://doi.org/10.1016/j.watres.2019.05.025>.
- Bourgin, M.; Beck, B.; Boehler, M.; Borowska, E.; Fleiner, J.; Salhi, E.; Teichler, R.; von Gunten, U.; Siegrist, H.; Mc Ardell, C.S. Evaluation of a full-scale wastewater treatment plant upgraded with ozonation and biological post-treatments: Abatement of

- micropollutants, formation of transformation products and oxidation by-products. *Water Res.* **2018**, *129*, 486–498. <https://doi.org/10.1016/j.watres.2017.10.036>.
20. EPA. Recreational Water Quality Criteria. Available online: <https://www.epa.gov/sites/production/files/2015-10/documents/rwqc2012.pdf> (accessed on 2 March 2021).
  21. Rojas-Valencia, M.N. Research on ozone application as disinfectant and action mechanisms on wastewater microorganisms. In *Science against Microbial Pathogens: Communicating Current Research and Technological Advances*; Microbiology Book Series-Number 3; FORMATEX: Badajoz, Spain, 2011; Volume 1, pp. 263–271.
  22. IARC Working Group on the Evaluation of Carcinogenic Risks to Humans. Carbon black, titanium dioxide and talc. *IARC Monogr. Eval. Carcinog. Risks Hum.* **2010**, *93*, 1–413.
  23. Moser, V.C.; Phillips, P.M.; Levine, A.B.; McDaniel, K.L.; Sills, R.C.; Jortner, B.S.; Butt, M.T. Neurotoxicity produced by dibromoacetic acid in drinking water of rats. *Toxicol. Sci.* **2004**, *79*, 112–122. <https://doi.org/10.1093/toxsci/kfh081>.
  24. Guariglia, S.R.; Jenkins, E.C.; Chadman, K.K.; Wen, G.Y. Chlorination byproducts induce gender specific autistic-like behaviors in CD-1 mice. *Neurotoxicology* **2011**, *32*, 545–553. <https://doi.org/10.1016/j.neuro.2011.06.008>.
  25. Manasfi, T.; Coulomb, B.; Boudenne, J.L. Occurrence, origin, and toxicity of disinfection byproducts in chlorinated swimming pools: An overview. *Int. J. Hyg. Environ. Health* **2017**, *220*, 591–603. <https://doi.org/10.1016/j.ijheh.2017.01.005>.
  26. Dong, G.; Chen, B.; Liu, B.; Hounjet, L.J.; Cao, Y.; Stoyanov, S.R.; Yang, M.; Zhang, B. Advanced oxidation processes in micro-reactors for water and wastewater treatment: Development, challenges, and opportunities. *Water Res.* **2022**, *211*, 118047. <https://doi.org/10.1016/j.watres.2022.118047>.
  27. Starling, M.C.V.M.; de Mendonça Neto, R.P.; Pires, G.F.F.; Vilela, P.B.; Amorim, C.C. Combat of antimicrobial resistance in municipal wastewater treatment plant effluent via solar advanced oxidation processes: Achievements and perspectives. *Sci. Total Environ.* **2021**, *786*, 147448. <https://doi.org/10.1016/j.scitotenv.2021.147448>.
  28. Wang, J.; Wang, S. Toxicity changes of wastewater during various advanced oxidation processes treatment: An overview. *J. Cleaner Prod.* **2021**, *315*, 128202. <https://doi.org/10.1016/j.jclepro.2021.128202>.
  29. Jamshaid, M.; Khan, I.M.; Fernandez, J.; Shanableh, A.; Hussaine, T.; ur Rehman, A. Synthesis of Ti<sup>4+</sup> doped Ca-BiFO<sub>3</sub> for the enhanced photodegradation of moxifloxacin. *New J. Chem.* **2022**, *46*, 19848–19856. <https://doi.org/10.1039/D2NJ03084E>.
  30. Jamshaid, M.; Khan, H.M.; Nazir, A.M.; Wattoo, A.M.; Shahzad, K.; Malik, M.; Rehman, U.A. A novel bentonite–cobalt doped bismuth ferrite nanoparticles with boosted visible light induced photodegradation of methyl orange: Synthesis, characterization and analysis of physiochemical changes. *Int. J. Environ. Anal. Chem.* **2022**, *102*, 1–16. <https://doi.org/10.1080/03067319.2022.2032014>.
  31. Jamshaid, M.; Nazir, A.M.; Najam, T.; Shah, A.S.S.; Khan, M.H.; ur Rehman, A. Facile synthesis of Yb<sup>3+</sup>-Zn<sup>2+</sup> substituted M type hexaferrites: Structural, electric and photocatalytic properties under visible light for methylene blue removal. *Chem. Phys. Lett.* **2022**, *805*, 139939.
  32. Paumo, H.K.; Dalhatou, S.; Katata-Seru, K.M.; Kamdem, B.P.; Tijani, J.O.; Vishwanathan, V.; Kane, A.; Bahadur, I. TiO<sub>2</sub> assisted photocatalysts for degradation of emerging organic pollutants in water and wastewater. *J. Mol. Liq.* **2021**, *331*, 115458. <https://doi.org/10.1016/j.molliq.2021.115458>.
  33. Özkal, C.B.; Venieri, D.; Gounaki, I.; Meric, S. Assessment of thin-film photocatalysis inactivation of different bacterial indicators and effect on their antibiotic resistance profile. *Appl. Catal. B* **2019**, *244*, 612–619. <https://doi.org/10.1016/j.apcatb.2018.11.095>.
  34. Gomes, J.; Lincho, J.; Domingues, E.; Quinta-Ferreira, R.M.; Martins, R.C. N–TiO<sub>2</sub> photocatalysts: A review of their characteristics and capacity for emerging contaminants removal. *Water* **2019**, *11*, 373. <https://doi.org/10.3390/w11020373>.
  35. He, J.; Kumar, A.; Khan, M.; Lo, I.M.C. Critical review of photocatalytic disinfection of bacteria: From noble metals- and carbon nanomaterials-TiO<sub>2</sub> composites to challenges of water characteristics and strategic solutions. *Sci. Total Environ.* **2021**, *758*, 143953. <https://doi.org/10.1016/j.scitotenv.2020.143953>.
  36. He, L.; Tan, T.; Gao, Z.; Fan, L. The shock effect of inorganic suspended solids in surface runoff on wastewater treatment plant performance. *Int. J. Environ. Res. Public Health* **2019**, *16*, 453. <https://doi.org/10.3390/ijerph16030453>.
  37. Kang, X.; Liu, S.; Dai, Z.; He, Y.; Song, X.; Tan, Z. Titanium dioxide: From engineering to applications. *Catalysts* **2019**, *9*, 191. <https://doi.org/10.3390/catal9020191>.
  38. Yi, H.; Huang, D.; Qin, L.; Zeng, G.; Lai, C.; Cheng, M.; Ye, S.; Song, B.; Ren, X.; Guo, X. Selective prepared carbon nanomaterials for advanced photocatalytic application in environmental pollutant treatment and hydrogen production. *Appl. Catal. B* **2018**, *239*, 408–424. <https://doi.org/10.1016/j.apcatb.2018.07.068>.
  39. He, J.; Zeng, X.; Lan, S.; Lo, I.M.C. Reusable magnetic Ag/Fe<sub>3</sub>N-TiO<sub>2</sub>/Fe<sub>3</sub>O<sub>4</sub>@SiO<sub>2</sub> composite for simultaneous photocatalytic disinfection of *E. coli* and degradation of bisphenol A in sewage under visible light. *Chemosphere* **2019**, *217*, 869–878. <https://doi.org/10.1016/j.chemosphere.2018.11.072>.
  40. Abdel-Raouf, N.; Al-Homaidan, A.A.; Ibraheem, I.B. Microalgae and wastewater treatment. *Saudi J. Biol. Sci.* **2012**, *19*, 257–275. <https://doi.org/10.1016/j.sjbs.2012.04.005>.
  41. Galata, E.; Georgakopoulou, E.A.; Kassalia, M.-E.; Papadopoulou-Fermeli, N.; Pavlatou, E.A. Development of smart composites based on doped-TiO<sub>2</sub> nanoparticles with visible light anticancer properties. *Materials* **2019**, *12*, 2589. <https://doi.org/10.3390/ma12162589>.
  42. Kuliesiene, N.; Sakalauskaitė, S.; Tuckute, S.; Urbonavicius, M.; Varnagiris, S.; Daugelavicius, R.; Lelis, M. TiO<sub>2</sub> application for the photocatalytic inactivation of *S. enterica*, *E. coli* and *M. luteus* bacteria mixtures. *Environ. Clim. Technol.* **2020**, *24*, 418–429. <https://doi.org/10.2478/rtulect-2020-0113>.



43. Tayade, R.J.; Surolia, P.K.; Kulkarni, R.G.; Jasra, R.V. Photocatalytic degradation of dyes and organic contaminants in water using nanocrystalline anatase and rutile TiO<sub>2</sub>. *Sci. Technol. Adv. Mater.* **2007**, *8*, 455–462. <https://doi.org/10.1016/j.stam.2007.05.006>.
44. Phomma, S.; Wutikhun, T.; Kasamechong, P.; Eksangsri, T.; Sapcharoenkun, C. Effect of calcination temperature on photocatalytic activity of synthesized TiO<sub>2</sub> nanoparticles via wet ball milling sol-gel method. *Appl. Sci.* **2020**, *10*, 993. <https://doi.org/10.3390/app10030993>.
45. Zhang, H.; Banfield, J.F. Understanding polymorphic phase transformation behavior during growth of nanocrystalline aggregates: insights from TiO<sub>2</sub>. *J. Phys. Chem. B* **2000**, *104*, 3481–3487. <https://doi.org/10.1021/jp000499j>.
46. Delgado-Díaz, D.; Hernández-Ramírez, A.; Guzmán-Mar, J.L.; Villanueva-Rodríguez, M.; Maya-Treviño, L.; Hinojosa-Reyes, L. N-S co-doped TiO<sub>2</sub> synthesized by microwave precipitation method: Effective photocatalytic performance for the removal of organoarsenic compounds. *J. Environ. Chem. Eng.* **2021**, *9*, 106683. <https://doi.org/10.1016/j.jece.2021.106683>.
47. Meng, Y. A sustainable approach to fabricating Ag nanoparticles/PVA hybrid nanofiber and its catalytic activity. *Nanomaterials* **2015**, *5*, 1124–1135. <https://doi.org/10.3390/nano5021124>.
48. Limón-Rocha, I.; Guzmán-González, C.A.; Anaya-Esparza, L.M.; Romero-Toledo, R.; Rico, J.L.; González-Vargas, O.A.; Pérez-Larios, A. Effect of the precursor on the synthesis of ZnO and its photocatalytic activity. *Inorganics* **2022**, *10*, 16. <https://doi.org/10.3390/inorganics10020016>.
49. Levin, A.A.; Narykova, M.V.; Lihachev, A.I.; Kardashev, B.K.; Kadomtsev, A.G.; Brunkov, P.N.; Panfilov, A.G.; Prasolov, N.D.; Sultanov, M.M.; Kuryanov, V.N.; et al. modification of the structural, microstructural, and elastoplastic properties of aluminum wires after operation. *Metals* **2021**, *11*, 1955. <https://doi.org/10.3390/met11121955>.
50. Lu, X.; Lv, X.; Sun, Z.; Zheng, Y. Nanocomposites of poly(l-lactide) and surface-grafted TiO<sub>2</sub> nanoparticles: Synthesis and characterization. *Eur. Polym. J.* **2008**, *44*, 2476–2481. <https://doi.org/10.1016/j.eurpolymj.2008.06.002>.
51. Praveen, P.; Viruthagiri, G.; Mugundan, S.; Shanmugam, N. Structural, optical and morphological analyses of pristine titanium di-oxide nanoparticles—Synthesized via sol-gel route. *Spectrochim. Acta Part A* **2014**, *117*, 622–629. <https://doi.org/10.1016/j.saa.2013.09.037>.
52. Olurode, K.; Neelgund, G.M.; Oki, A.; Luo, Z. A facile hydrothermal approach for construction of carbon coating on TiO<sub>2</sub> nanoparticles. *Spectrochim. Acta Part A* **2012**, *89*, 333–336. <https://doi.org/10.1016/j.saa.2011.12.025>.
53. Ščepanovi, M.; Aškračić, S.; Berec, V.; Golubović, A.; Dohčević-Mitrović, Z.; Kremenović, A.; Popović, Z.V. Characterization of La-doped TiO<sub>2</sub> nanopowders by Raman spectroscopy. *Acta Phys. Pol. A* **2009**, *115*, 771–774. <https://doi.org/10.12693/APhysPolA.115.771>.
54. Al-Arjan, W.S. Zinc oxide nanoparticles and their application in adsorption of toxic dye from aqueous solution. *Polymers* **2022**, *14*, 3086. <https://doi.org/10.3390/polym14153086>.
55. Thommes, M.; Kaneko, K.; Neimark, A.; Olivier, J.; Rodriguez-Reinoso, F.; Rouquerol, J.; Sing, K. Physisorption of gases, with special reference to the evaluation of surface area and pore size distribution (IUPAC Technical Report). *Pure Appl. Chem.* **2015**, *87*, 1051–1069. <https://doi.org/10.1515/pac-2014-1117>.
56. Turcu, E.; Coromelci, C.G.; Harabagiu, V.; Ignat, M. Enhancing the photocatalytic activity of TiO<sub>2</sub> for the degradation of congo red dye by adjusting the ultrasonication regime applied in its synthesis procedure. *Catalysts* **2023**, *13*, 345. <https://doi.org/10.3390/catal13020345>.
57. Wang, X.; Pehkonen, O.S.; Rämö, J.; Väänänen, M.; Highfielde, J.G.; Laasonen, K. Experimental and computational studies of nitrogen doped Degussa P25 TiO<sub>2</sub>: Application to visible-light driven photo-oxidation of As (III). *Catal. Sci. Technol.* **2012**, *2*, 784–793. <https://doi.org/10.1039/C2CY00486K>.
58. Amorós-Pérez, A.; Cano-Casanova, L.; Castillo-Deltell, A.; Lillo-Ródenas, M.Á.; Román-Martínez, M.d.C. TiO<sub>2</sub> modification with transition metallic species (Cr, Co, Ni, and Cu) for photocatalytic abatement of acetic acid in liquid phase and propene in gas phase. *Materials* **2019**, *12*, 40. <https://doi.org/10.3390/ma12010040>.
59. Zaky, A.A.; Christopoulos, E.; Gkini, K.; Arfanis, M.K.; Sygellou, L.; Kaltzoglou, A.; Stergiou, A.; Tagmatarchis, N.; Balis, N.; Falaras, P. Enhancing efficiency and decreasing photocatalytic degradation of perovskite solar cells using a hydrophobic copper-modified titania electron transport layer. *Appl. Catal. B* **2021**, *284*, 119714. <https://doi.org/10.1016/j.apcatb.2020.119714>.
60. Beraneka, R.; Kisch, H. Tuning the optical and photoelectrochemical properties of surface-modified TiO<sub>2</sub>. *Photochem. Photobiol. Sci.* **2008**, *7*, 40–48. <https://doi.org/10.1039/B711658F>.
61. Piątkowska, A.; Janus, M.; Szymański, K.; Mozia, S. C-, N- and S-doped TiO<sub>2</sub> photocatalysts: A review. *Catalysts* **2021**, *11*, 144. <https://doi.org/10.3390/catal11010144>.
62. Kassalia, M.-E.; Nikolaou, Z.; Pavlatou, E.A. Photocatalytic testing protocol for N-doped TiO<sub>2</sub> nanostructured particles under visible light irradiation using the statistical Taguchi experimental design. *Appl. Sci.* **2023**, *13*, 774. <https://doi.org/10.3390/app13020774>.
63. Aspromonte, S.G.; Mizrahi, M.D.; Schneeberger, F.A.; Ramallo López, J.M.; Boix, A.V. Study of the nature and location of silver in Ag-exchanged mordenite catalysts. Characterization by spectroscopic techniques. *J. Phys. Chem. C* **2013**, *117*, 25433–25442. <https://doi.org/10.1021/jp4046269>.
64. Henderson, A.; Briggs, D.; Vickerman, J. *The XPS of Polymers Database*, version 1.0; SurfaceSpectra Ltd.: Manchester, UK, 2000.
65. Cant, D.J.H.; Syres, K.L.; Lunt, P.J.B.; Radtke, H.; Treacy, J.; Thomas, P.J.; Lewis, E.A.; Haigh, S.J.; O'Brien, P.; Schulte, K.; et al. Surface properties of nanocrystalline PbS films deposited at the water–oil interface: A study of atmospheric aging. *Langmuir* **2015**, *31*, 1445–1453. <https://doi.org/10.1021/la504779h>.

66. Sun, M.; Fang, Y.; Sun, S.; Wang, Y. Surface co-modification of TiO<sub>2</sub> with N doping and Ag loading for enhanced visible-light photoactivity. *RSC Adv.* **2016**, *6*, 12272–12279. <https://doi.org/10.1039/c5ra23593f>.
67. Motzkus, C.; Macé, T.; Vaslin-Reimann, S.; Ausset, P.; Maillé, M. Characterization of manufactured TiO<sub>2</sub> nanoparticles. *J. Phys. Conf. Ser.* **2013**, *429*, 012012. <https://doi.org/10.1088/1742-6596/429/1/012012>.
68. Gatou, M.-A.; Lagopati, N.; Vagena, I.-A.; Gazouli, M.; Pavlatou, E.A. ZnO nanoparticles from different precursors and their photocatalytic potential for biomedical use. *Nanomaterials* **2023**, *13*, 122. <https://doi.org/10.3390/nano13010122>.
69. Fu, H.; Pan, Ch.; Yao, W.; Zhu, Y. Visible-light-induced degradation of Rhodamine B by nanosized Bi<sub>2</sub>WO<sub>6</sub>. *J. Phys. Chem. B* **2005**, *109*, 22432–22439. <https://doi.org/10.1021/jp052995j>.
70. Hu, X.; Mohamood, T.; Ma, W.; Chen, C.; Zhao, J. Oxidative decomposition of Rhodamine B dye in the presence of VO<sup>2+</sup> and/or Pt(IV) under visible light irradiation: N-deethylation, chromophore cleavage and mineralization. *J. Phys. Chem. B* **2006**, *110*, 26012–26018. <https://doi.org/10.1021/jp063588q>.
71. Liu, G.; Li, X.; Zhao, J.; Hidaka, H.; Serpone, N. Photooxidation pathway of sulforhodamine-B. Dependence on the adsorption mode on TiO<sub>2</sub> exposed to visible light radiation. *Environ. Sci. Technol.* **2000**, *34*, 18, 3982–3990. <https://doi.org/10.1021/es001064c>.
72. Ali, T.; Tripathi, P.; Azam, A.; Raza, W.; Ahmed, A.S.; Ahmed, A.; Muneer, M. Photocatalytic performance of Fe-doped TiO<sub>2</sub> nanoparticles under visible-light irradiation. *Mater. Res. Express.* **2017**, *4*, 12. <https://doi.org/10.1088/2053-1591/aa576d>.
73. Cong, Y.; Zhang, J.; Chen, F.; Anpo, M.; He, D. Preparation, photocatalytic activity, and mechanism of nano-TiO<sub>2</sub> co-doped with nitrogen and iron (III). *J. Phys. Chem. C* **2007**, *111*, 10618–10623. <https://doi.org/10.1021/jp0727493>.
74. Uribe-López, M.C.; Hidalgo-López, M.C.; López-González, R.; Frías-Márquez, D.M.; Núñez-Nogueira, G.; Hernández-Castillo, D.; Alvarez-Lemus, M.A. Photocatalytic activity of ZnO nanoparticles and the role of the synthesis method on their physical and chemical properties. *J. Photochem. Photobiol. A* **2021**, *404*, 112866. <https://doi.org/10.1016/j.jphotochem.2020.112866>.
75. Peter, I.J.; Praveen, E.; Vignesh, G.; Nithiananthi, P. ZnO nanostructures with different morphology for enhanced photocatalytic activity. *Mater. Res. Express* **2017**, *4*, 124003. <https://doi.org/10.1088/2053-1591/aa9d5d>.
76. Wen, Y.; Ding, H.; Shana, Y. Preparation and visible light photocatalytic activity of Ag/TiO<sub>2</sub>/graphene nanocomposite. *Nanoscale* **2011**, *3*, 4411–4417. <https://doi.org/10.1039/C1NR10604J>.
77. Umabayashi, T.; Yamaki, T.; Tanaka, S.; Asai, K. Visible Light-induced degradation of Methylene Blue on S-doped TiO<sub>2</sub>. *Chem. Lett.* **2003**, *32*, 330–331. <https://doi.org/10.1246/cl.2003.330>.
78. Brindha, A.; Sivakumar, T. Visible active N, S co-doped TiO<sub>2</sub>/graphene photocatalysts for the degradation of hazardous dyes. *J. Photochem. Photobiol. A* **2017**, *340*, 146–156. <https://doi.org/10.1016/j.jphotochem.2017.03.010>.
79. Zarrabi, M.; Entezari, M.H.; Goharshadic, E.K. Photocatalytic oxidative desulfurization of dibenzothiophene by C/TiO<sub>2</sub>@MCM-41 nanoparticles under visible light and mild conditions. *RSC Adv.* **2015**, *5*, 34652–34662. <https://doi.org/10.1039/C5RA02513C>.
80. Zhao, C.; Pelaez, M.; Dionysiou, D.D.; Pillai, S.C.; Byrne, J.A.; O’Shea, K.E. UV and visible light activated TiO<sub>2</sub> photocatalysis of 6-hydroxymethyl uracil, a model compound for the potent cyanotoxin cylindrospermopsin. *Catal. Today* **2014**, *224*, 70–76. <https://doi.org/10.1016/j.cattod.2013.09.042>.
81. Cho, M.; Chung, H.; Choi, W.; Yoon, J. Different inactivation behaviors of MS-2 phage and Escherichia coli in TiO<sub>2</sub> photocatalytic disinfection. *Appl. Environ. Microbiol.* **2005**, *71*, 270–275. <https://doi.org/10.1128/AEM.71.1.270-275.2005>.
82. Cho, M.; Chung, H.; Choi, W.; Yoon, J. Linear correlation between inactivation of *E. coli* and OH radical concentration in TiO<sub>2</sub> photocatalytic disinfection. *Water Res.* **2004**, *38*, 1069–1077. <https://doi.org/10.1016/j.watres.2003.10.029>.
83. Paleologou, A.; Marakas, H.; Xekoukoulotakis, N.P.; Moya, A.; Vergara, Y.; Kalogerakis, N.; Gikas, P.; Mantzavinos, D. Disinfection of water and wastewater by TiO<sub>2</sub> photocatalysis, sonolysis and UV-C irradiation. *Catal. Today* **2017**, *129*, 136–142. <https://doi.org/10.1016/j.cattod.2007.06.059>.
84. Rincón, A.-G.; Pulgarin, C. Comparative evaluation of Fe<sup>3+</sup> and TiO<sub>2</sub> photoassisted processes in solar photocatalytic disinfection of water. *Appl. Catal. B* **2006**, *63*, 222–231.
85. Rincón, A.G.; Pulgarin, C. Effect of pH, inorganic ions, organic matter and H<sub>2</sub>O<sub>2</sub> on *E. coli* K12 photocatalytic inactivation by TiO<sub>2</sub>: Implications in solar water disinfection. *Appl. Catal. B* **2004**, *51*, 283–302.
86. Sunada, K.; Watanabe, T.; Hashimoto, K. Studies on photokilling of bacteria on TiO<sub>2</sub> thin film. *J. Photochem. Photobiol. A* **2003**, *156*, 227–233. [https://doi.org/10.1016/S1010-6030\(02\)00434-3](https://doi.org/10.1016/S1010-6030(02)00434-3).
87. Huang, Z.; Maness, P.-C.; Blake, D.M.; Wolfrum, E.J.; Smolinski, S.L.; Jacoby, W.A. Bactericidal mode of titanium dioxide photocatalysis. *J. Photochem. Photobiol. A* **2000**, *130*, 163–170.
88. Wang, L.; Li, B.; Dionysiou, D.D.; Chen, B.; Yang, J.; Li, J. Overlooked formation of H<sub>2</sub>O<sub>2</sub> during the hydroxyl radical-scavenging process when using alcohols as scavengers. *Environ. Sci. Technol.* **2022**, *56*, 3386–3396. <https://doi.org/10.1021/acs.est.1c03796>.
89. Trenczek-Zajac, A.; Synowiec, M.; Zakrzewska, K.; Zazakowny, K.; Kowalski, K.; Dziedzic, A.; Radecka, M. Scavenger-supported photocatalytic evidence of an extended Type I electronic structure of the TiO<sub>2</sub>@Fe<sub>2</sub>O<sub>3</sub> interface. *ACS Appl. Mater. Interfaces* **2022**, *14*, 38255–38269. <https://doi.org/10.1021/acsami.2c06404>.
90. Araña, J.; Tello Rendón, E.; Doña Rodríguez, J.M.; Herrera Melián, J.A.; González Díaz, O.; Pérez Peña, J. High concentrated phenol and 1,2-propylene glycol water solutions treatment by photocatalysis: Catalyst recovery and re-use. *Appl. Catal. B Environ.* **2001**, *30*, 1–10. [https://doi.org/10.1016/S0926-3373\(00\)00218-6](https://doi.org/10.1016/S0926-3373(00)00218-6).
91. Farhadian, N.; Akbarzadeh, R.; Pirsahab, M.; Jen, T.-C.; Fakhri, Y.; Asadi, A. Chitosan modified N, S-doped TiO<sub>2</sub> and N, S-doped ZnO for visible light photocatalytic degradation of tetracycline. *Int. J. Biol. Macromol.* **2019**, *132*, 360–373. <https://doi.org/10.1016/j.ijbiomac.2019.03.217>.

92. Eslami, A.; Amini, M.M.; Yazdanbakhsh, A.R.; Mohseni-Bandpei, A.; Safari, A.A.; Asadi, A. N,S co-doped TiO<sub>2</sub> nanoparticles and nanosheets in simulated solar light for photocatalytic degradation of non-steroidal anti-inflammatory drugs in water: A comparative study. *J. Chem. Technol. Biotechnol.* **2016**, *91*, 2693–2704. <https://doi.org/10.1002/jctb.4877>.
93. Iskandar, F.; Nandiyanto, A.B.D.; Yun, K.M.; Hogan, C.J., Jr.; Okuyama, K.; Biswas, P. Enhanced photocatalytic performance of brookite TiO<sub>2</sub> macroporous particles prepared by spray drying with colloidal templating. *Adv. Mater.* **2007**, *19*, 1408–1412. <https://doi.org/10.1002/adma.200601822>.
94. Levard, C.; Mitra, S.; Yang, T.; Jew, A.D.; Badireddy, A.R.; Lowry, G.V.; Brown, G.E., Jr. Effect of chloride on the dissolution rate of silver nanoparticles and toxicity to *E. coli*. *Environ. Sci. Technol.* **2013**, *47*, 5738–5745. <https://doi.org/10.1021/es400396f>.
95. Peng, S.; Chen, Y.; Jin, X.; Lu, W.; Gou, M.; Wei, X.; Xie, J. Polyimide with half encapsulated silver nanoparticles grafted ceramic composite membrane: Enhanced silver stability and lasting anti-biofouling performance. *J. Membr. Sci.* **2020**, *611*, 118340. <https://doi.org/10.1016/j.memsci.2020.118340>.

**Disclaimer/Publisher's Note:** The statements, opinions and data contained in all publications are solely those of the individual author(s) and contributor(s) and not of MDPI and/or the editor(s). MDPI and/or the editor(s) disclaim responsibility for any injury to people or property resulting from any ideas, methods, instructions or products referred to in the content.